nature astronomy

Article

https://doi.org/10.1038/s41550-023-02178-4

X-ray eruptions every 22 days from the nucleus of a nearby galaxy

Received: 10 March 2023

Accepted: 5 December 2023

Published online: 12 January 2024

Check for updates

Muryel Guolo[1] ✉, **Dheeraj R. Pasham**[2], **Michal Zajaček**[3], **Eric R. Coughlin**[4], **Suvi Gezari**[1,5], **Petra Suková**[6], **Thomas Wevers**[5,7], **Vojtěch Witzany**[8], **Francesco Tombesi**[9,10,11,12,13], **Sjoert van Velzen**[14], **Kate D. Alexander**[15], **Yuhan Yao**[16,17], **Riccardo Arcodia**[2], **Vladimír Karas**[6], **James C. A. Miller-Jones**[18], **Ronald Remillard**[2], **Keith Gendreau**[13] & **Elizabeth C. Ferrara**[12,13,19]

Galactic nuclei showing recurrent phases of activity and quiescence have recently been discovered. Some have recurrence times as short as a few hours to a day and are known as quasi-periodic X-ray eruption (QPE) sources. Others have recurrence times as long as hundreds to a thousand days and are called repeating nuclear transients. Here we present a multiwavelength overview of Swift J023017.0+283603 (hereafter Swift J0230+28), a source from which repeating and quasi-periodic X-ray flares are emitted from the nucleus of a previously unremarkable galaxy at ~165 Mpc. It has a recurrence time of approximately 22 days, an intermediary timescale between known repeating nuclear transients and QPE sources. The source also shows transient radio emission, likely associated with the X-ray emission. Such recurrent soft X-ray eruptions, with no accompanying ultraviolet or optical emission, are strikingly similar to QPE sources. However, in addition to having a recurrence time that is ~25 times longer than the longest-known QPE source, Swift J0230+28's eruptions exhibit somewhat distinct shapes and temperature evolution compared to the known QPE sources. Scenarios involving extreme mass ratio inspirals are favoured over disk instability models. The source reveals an unexplored timescale for repeating extragalactic transients and highlights the need for a wide-field, time-domain X-ray mission to explore the parameter space of recurring X-ray transients.

The field of view of Swift J023017.0+283603 (hereafter Swift J0230+28) was first observed by the Neil Gehrels Swift Observatory X-Ray Telescope (XRT) between December 2021 and January 2022 following the discovery of the supernova SN2021afkk (ref. 1), which is ~4' from Swift J0230+28. During that time, no X-ray emission was detected from the position of Swift J0230+28 (stacked upper-limit 0.3–2.0 keV flux of 2×10^{-14} erg s^{-1} cm^{-2}). However, an observation taken on 22 June 2022 and processed by the Swift live catalogue of transients[2,3] revealed an X-ray source with a 0.3–2.0 keV flux of 7×10^{-13} erg s^{-1} cm^{-2}, suggesting an enhancement of more than a factor of 35 (ref. 4). The X-ray spectrum was soft and thermal with a temperature of 121^{+13}_{-25} eV ($1.4^{+0.2}_{-0.3} \times 10^{6}$ K). Based on the spatial coincidence of the source with the centre of a nearby galaxy, the soft/thermal X-ray spectrum and the lack of any previous X-ray detection ('Constraints on the start of the eruptions' and Extended Data Fig. 1), it was initially reported[4,5] to be a flare resulting from the tidal disruption of a star by a massive black hole (MBH).

Monitoring of Swift J0230+28 with Swift/XRT between June and August of 2022 (modified Julian date (MJD) 59,752–59,798) revealed X-ray eruptions (increases in the 0.3–2.0 keV X-ray flux from non-detection to peaks of a factor of up to 100 higher than the upper

A full list of affiliations appears at the end of the paper. ✉e-mail: mguolop1@jhu.edu

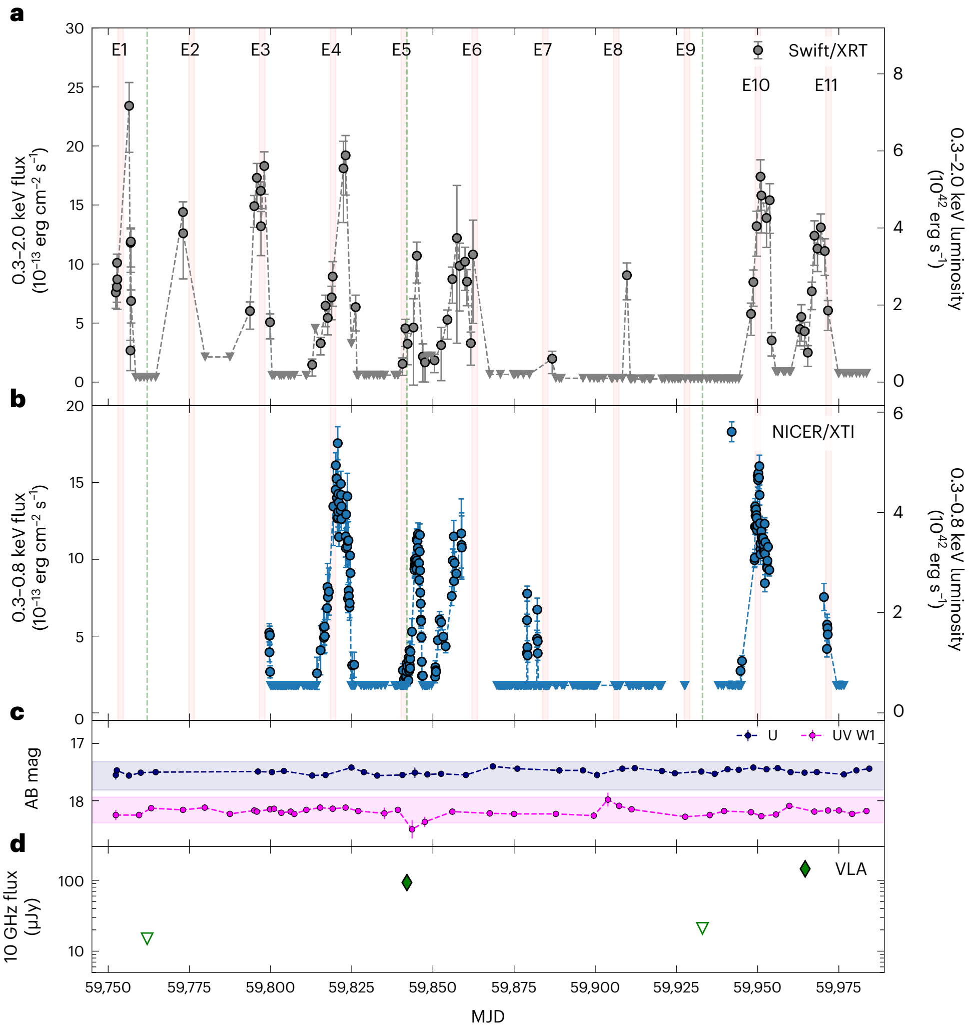

Fig. 1 | Light curves of Swift J0230+28. **a**, Swift/XRT 0.3–2.0 keV flux and luminosity evolution. Stacked 3σ upper limits between the eruptions are 2×10^{-14} erg s^{-1} cm^{-2}. **b**, NICER 0.3–0.8 keV flux and luminosity evolution. In **a** and **b**, circles are detections, reverse triangles are 3σ upper limits of non-detections and shaded pink regions indicate the $21.8^{+1.2}_{-0.5}$ days peak period found in the LSP analysis ('Time-resolved X-ray analyses'). **c**,**d**, UV/optical (**c**) and radio light curves (**d**). Swift/UVOT UV W1 and U bands are, respectively, dark blue and magenta points. The shaded region represents the ±2σ dispersion of the magnitude before the start of the X-ray eruptions (December 2021 to January 2022). Radio VLA observations are shown as green diamonds (detection) and inverse triangles (non-detection upper limits). Green dashed lines in **a** and **b** mark the epochs of the radio observations for reference. Error bars represent 1σ uncertainties in all panels. XTI, X-ray timing instrument.

limits) that lasted several days and were separated by longer periods (≳15 days) of non-detections (Fig. 1a). The X-ray eruptions had no accompanying changes in the optical and the ultraviolet (UV) bands (upper limit in the host-subtracted UV luminosity $\lesssim 3\times10^{42}$ erg s^{-1}; see 'UV/optical and radio counterparts'). These properties exclude the interpretation of a classical tidal disruption event (TDE; for example, [6–9]). Following the indication of these recurrent X-ray eruptions, we initiated a high-cadence monitoring programme with the Neutron Star Interior Composition Explorer (NICER) starting on MJD 59,798 as well as multiwavelength follow-ups with several other facilities ('Observations and data analysis').

In the 8 months following Swift J0230+28's discovery, Swift/XRT observed the source with an approximately daily cadence for a total of ~160 ks. Moreover, NICER observed the source several times per day—albeit with some gaps—for a total of ~500 ks. The monitoring campaign confirmed the recurrence of several X-ray eruptions, which, apparently, were repeating every ~3 weeks, as shown in Fig. 1. The Lomb–Scargle periodogram (LSP; refs. 10,11) of the resulting light curve (Fig. 2) has a strong peak at $21.8^{+1.2}_{-0.5}$ days, which indicates that the eruptions are quasi-periodic in nature. The pink shaded regions in Fig. 1 mark time intervals separated by the $21.8^{+1.2}_{-0.5}$ d period, which are referred to as epochs (E), from E1, E2, …, E11, during the ~240 d of monitoring.

Around most of the marked epochs, namely E1–E6, E10 and E11, Swift J0230+28 showed high-amplitude eruptions with a mean full-width at half-maximum (FWHM) duration of ~4.5 days (Supplementary Table 1). However, around E7 and E8, instead of the few-days-long eruptions, short-lived (<1 day) and lower-amplitude eruptions were observed. Furthermore, no X-ray detections were observed around E9, although extremely short-lived eruptions cannot be excluded given the lack of high-cadence NICER observations at the time. This indicates that, although the eruptions of Swift J0230+28 are quasi-periodic, there is a certain degree of irregularity in the system's periodicity and amplitude. The eruptions of Swift J0230+28 are slightly asymmetric; an asymmetric Gaussian profile fitted to the shape of the well-sampled and days-long eruptions shows that the rises are ~30% longer than the decays ('X-ray light curve' and Extended Data Fig. 2).

The high count rate obtained by NICER allowed us to perform time-resolved spectral analyses during the eruptions ('Time-resolved

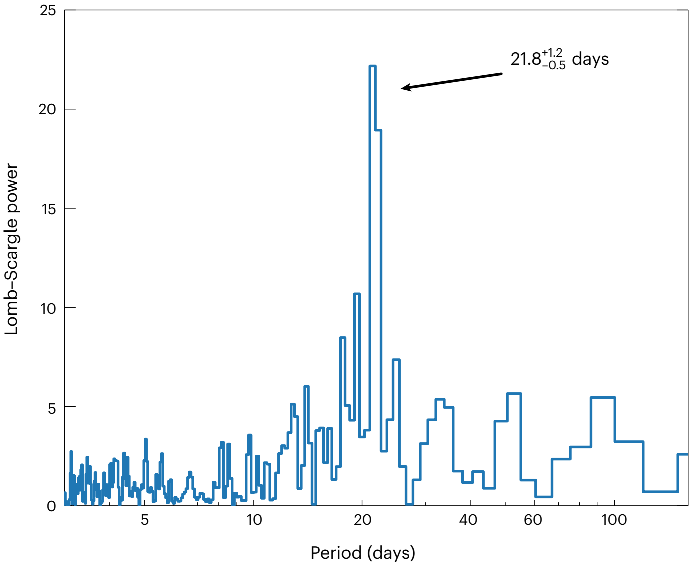

Fig. 2 | LSP for the Swift J0230+28 light curve. The two consecutive peak bins represent a period of $21.8^{+1.2}_{-0.5}$ days.

X-ray analyses'). The X-ray spectra are soft and no photons were detected at energies greater than 1.5 keV over all eruptions. A thermal model modified by absorption—both Galactic and intrinsic (column density $N_{\mathrm{H}} \approx 1$–3×10^{20} cm^{-2})—fits the spectra reasonably well with reduced χ^2 in the range (0.9, 1.9), as shown in Fig. 3 and Extended Data Fig. 3. The best-fitting temperature varied with time (Fig. 4 and Extended Data Table 1) and has a mean (standard deviation) of 160 eV (50 eV). The variation in temperature correlates with the evolution of the eruptions: a simple regression between temperature (T) and 0.3–0.8 keV X-ray luminosity (L) shows a correlation in the form $L \propto T^{1.9\pm0.5}$. However, note that the large spread occurred because Swift J0230+28 does not show a cool to warm to cool temperature evolution in each eruption. The temperature increased from the rise (~100 eV) to the peak (~150 eV) of the eruptions, but instead of decreasing during the decay (as one would expect for a direct correlation between temperature and luminosity), it continued to increase, up to ~200 eV. Hence, it has a cool to warm temperature evolution.

Our radio monitoring ('Very Large Array' and Extended Data Fig. 4) shows a transient point-like source at Swift J0230+28's position. Although the first and third observations (MJD 59,762 and MJD 59,933) showed no detections with 3σ upper limits of 15 and 25 μJy, respectively, our second visit on MJD 59,842 had a detection with a flux of 93 ± 7 μJy. This radio detection coincided with one of the X-ray eruptions, and the two radio non-detections coincided with X-ray quiescent phases, suggesting that the X-ray eruptions may be accompanied by radio emission (Fig. 1).

The position derived from XRT for Swift J0230+28 is consistent with the nucleus (0.2" ± 3.6", 90% uncertainty, from the photometric centre) of a spiral galaxy (Extended Data Fig. 5) at 165 Mpc ($z = 0.036$). The host galaxy is not in any active galactic nuclei (AGNs) catalogue, and there is no archival detection in X-ray or in radio bands before the start of the eruptions. The host also shows no infrared (IR) photometric excess nor any variability in the IR bands that would indicate the presence of a hot dust component (a 'torus'). However, optical emission-line diagnostic diagrams (Extended Data Fig. 6) based on nuclear spectra indicate the presence of a weak AGN (or low-luminosity AGN, LLAGN). The high-resolution optical spectrum of the nuclear region also allowed us to measure the stellar population velocity dispersion (σ_*) and estimate a black hole mass (M_{BH}) of $\log(M_{\mathrm{BH}}/M_\odot) = 6.6 \pm 0.4$, where $M_\odot$ is one solar mass, using the standard M_{BH} versus σ_* relation[12], which is in agreement with the M_{BH} derived from the host-galaxy mass (M_*; Extended Data Fig. 7), assuming the M_{BH} versus M_* relation of ref. 13. Based on the [O III] emission line and the 2–10 keV luminosity upper limit, we estimated the upper limit for the bolometric luminosity of the AGN (before the start of the eruptions) to be $L_{\mathrm{quiet,bol}} \leq 9 \times 10^{41}$ erg s^{-1}, which for the estimated black hole mass translates into an Eddington ratio $\lambda_{\mathrm{Edd}} = L_{\mathrm{quiet,bol}}/L_{\mathrm{Edd}} < 0.002$, supporting the LLAGN classification by the line ratio diagnostic diagrams ('The host galaxy'). At such a low accretion rate, a standard thin accretion disk should not be present in Swift J0230+28's host. Instead, any accretion flow, if present, is more probably dominated by advection.

The recurrent phases of high activity followed by phases of quiescence, could, in principle, classify Swift J0230+28 as a repeating nuclear transient (RNT). Three clear cases of RNTs are known: ASASSN-14ko (ref. 14), eRASStJ045650.3-203750 (hereafter eRA J0456-20; ref. 15) and AT2018fyk (ref. 16). These sources show repeated flares with recurrence times varying from 114 to 1,200 days (see Supplementary Information, 'Repeating Nuclear Transients and Swift J0230+28' for detailed properties of these sources) and are interpreted by most studies as the result of a star being repeatedly partially disrupted by a central MBH[14–18]. However, Swift J0230+28 differs notably from RNTs in the following ways: (1) RNTs exhibit much brighter X-ray luminosities compared to Swift J0230+28. (2) RNTs are even brighter in the UV and optical bands than in X-rays, whereas no UV or optical emission has

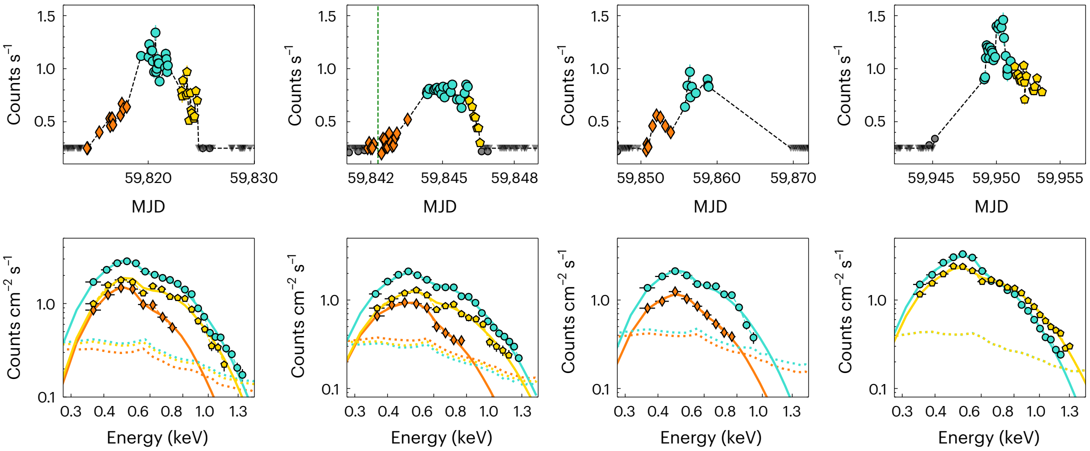

Fig. 3 | NICER time-resolved spectroscopy. Top, well-sampled NICER light curves of four eruptions. Orange, cyan and gold mark the observations stacked to create rise, peak and decay spectra. The green dashed vertical line marks the epoch of the radio detection. Bottom, observed spectra (markers) and best-fitting thermal model (continuous lines) and background spectra (dotted lines). Error bars represent 1σ uncertainties in all panels.

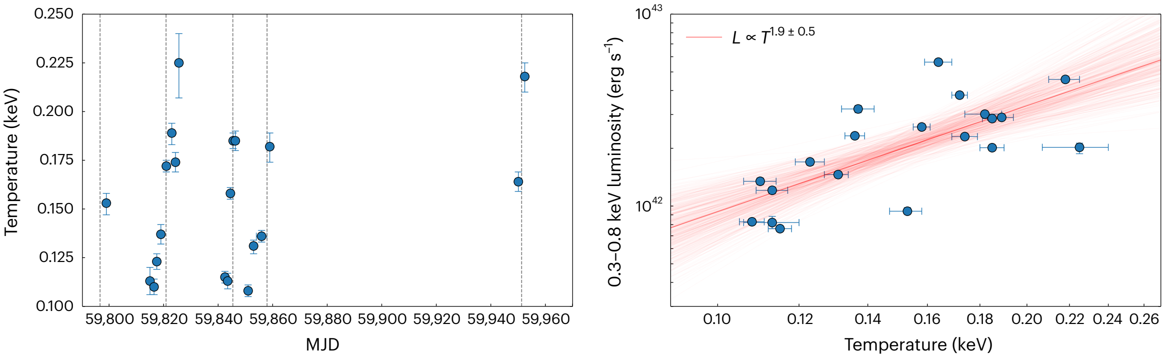

Fig. 4 | Time-resolved spectral properties. Left, evolution of the temperature (T_{in}, using diskbb). Right, 0.3–0.8 keV luminosity (NICER) as a function of the temperature. Red lines are samples drawn from the posterior distributions of the best-fitting regression, $L \propto T^{1.9\pm0.5}$. Error bars represent 1σ uncertainty.

been detected for Swift J0230+28. (3) RNTs have rapid rises and much slower decays, whereas Swift J0230+28's eruptions have a slightly slower rise than decay. (4) None of the RNTs show a purely soft, thermal X-ray spectrum, unlike Swift J0230+28.

Swift J0230+28's recurrent soft X-ray eruptions from the nucleus of a galaxy hosting a relatively small black hole ($M_{\mathrm{BH}} \leq 10^{6.6}\,M_{\odot}$), with no accompanying UV or optical emission, are characteristic of the recently discovered class of quasi-periodic X-ray eruption (QPE) sources. Four confirmed QPE sources are known: GSN 069 (ref. 19). RX J1301 (ref. 20), eRO-QPE1 and eRO-QPE2 (ref. 21). A detailed description of their properties is presented in Supplementary Information, 'Quasi-periodic erupters and Swift J0230+28'. However, the known QPE sources show much shorter mean recurrence times than Swift J0230+28, from a few hours to ~1 d (see Extended Data Table 2 for exact values and Extended Data Fig. 8 for a comparison of light curves). This could indicate that Swift J0230+28 may be a QPE source with a longer timescale (~25 times longer than eRO-QPE1). However, as discussed in detail in Supplementary Information, 'Quasi-periodic erupters and Swift J0230+28', Swift J0230+28 possesses some properties that differentiate it from, and makes it unique compared to, the four known sources of QPEs: (1) In each of their eruptions, the four QPE sources showed a cool to warm to cool temperature evolution, whereas Swift J0230+28 did not cool during the decay of its eruptions. Instead, the temperature increased continuously until the source faded below the level of detectability. (2) The shapes of the eruptions for these four QPE sources are either nearly symmetric or slightly asymmetric with longer decays than rises, whereas the rises of Swift J0230+28 are ~30% longer than the decays.

A comparison between the general properties of Swift J0230+28, RNTs and QPEs is shown in Table 1. In summary, Swift J0230+28 has more similarities with QPEs than with RNTs. It shares many, but not all, of the properties of known QPE sources and operates on an order-of-magnitude longer timescale. Observationally, it resembles either a long timescale QPE source, with slightly distinct properties, or the first example of a completely new class of transient with other members yet to be discovered. If the former is assumed, one can investigate how Swift J0230+28's properties relate to those of the four known QPE sources. Figure 5 shows that the recurrence time and the duration of the X-ray eruptions seem to be correlated, with a duty cycle (ratio of the duration and recurrence time) equal to 0.24 ± 0.13. A positive correlation also appears to be present between the recurrence time and amplitude of the eruptions, although only lower limits for Swift J0230+28's amplitudes are known. However, the timing properties (duration and recurrence time) do not seem to be correlated with M_{BH}, perhaps indicating that the timescales of quasi-periodic, soft X-ray eruptions do not depend on M_{BH}.

Table 1 | General properties of Swift J0230+28 compared to QPEs and RNTs

Properties	Swift J0230+28	QPEs	RNTs
Recurrent soft X-ray eruptions	Yes	Yes	No[a]
Mean recurrence time	~22 days	2.4–18.5 h	114–1,200 days
X-ray spectra	Soft and thermal	Soft and thermal	Soft and thermal including from the corona or from only the corona
X-ray luminosity at peak[b] (erg s^{-1})	A few ×10^{42}	10^{42}–10^{43}	Morer than a few ×10^{43}
UV or optical emission	No	No	Yes
UV or optical luminosity at peak (erg s^{-1})	<3×10^{42}; see [c]	≪10^{43}; see [d]	≥10^{44}
Light curve shape	Slightly asymmetric (rises ~30% longer than decays)	Symmetric or slightly asymmetric (longer decays than rises)	Complex and varied[e]
M_{BH}	$10^{6.6}\,M_{\odot}$	10^{5}–$10^{6.6}\,M_{\odot}$	$10^{7.1}$–$10^{7.7}\,M_{\odot}$

QPEs are GSN 069 (ref. 19), RX J1301 (ref. 20), eRO-QPE1 and eRO-QPE2 (ref. 21). RNTs are ASASSN-14ko (ref. 14), eRA J0456-20 (ref. 15) and AT2018fyk (ref. 16). [a]The outbursts of eRA J0456-20 evolved much smoothly than the eruptions of QPEs or Swift J0230+28. The periodic behaviour of ASASSN-14ko was mostly observed in the UV and optical bands and less so in X-rays. The X-ray spectra of all three RNTs are not soft but show hard X-ray emission from the corona. [b]In the 0.3–2.0 keV band for Swift J0230+28 and QPEs and in the 0.3–10 keV band for RNTs. [c]Based on the lack of variability in Swift/UVOT bands ('UV/optical and radio counterparts'). [d]Based on the lack of variability in data from Swift/UVOT and XMM-Newton/OM instruments from the host level. [e]ASASNN-14ko and AT2018fyk are like TDEs (with a rapid rise and a decay several times longer). eRA J0456-20 has much longer rises than decays.

Several models have been proposed to explain the repeating and recurrent phases of nuclear activity in RNTs and QPE sources, and those models can be roughly divided into two classes: those involving accretion-disk instabilities and those with smaller-mass bodies orbiting a MBH (leading to extreme mass ratio inspirals; EMRIs). A more detailed discussion of each of these classes of models, and their strengths and weaknesses in explaining Swift J0230+28's properties, are presented in Supplementary Information, 'Physical models for Swift J0230+28', but in the following, we summarize some of their aspects.

Some studies of accretion-disk-driven models have proposed that instabilities associated with the inner accretion flow, from precession[22–25] to distinct types of pressure or ionization instabilities[26–30], could produce quasi-periodic phases of high and low activity. However,

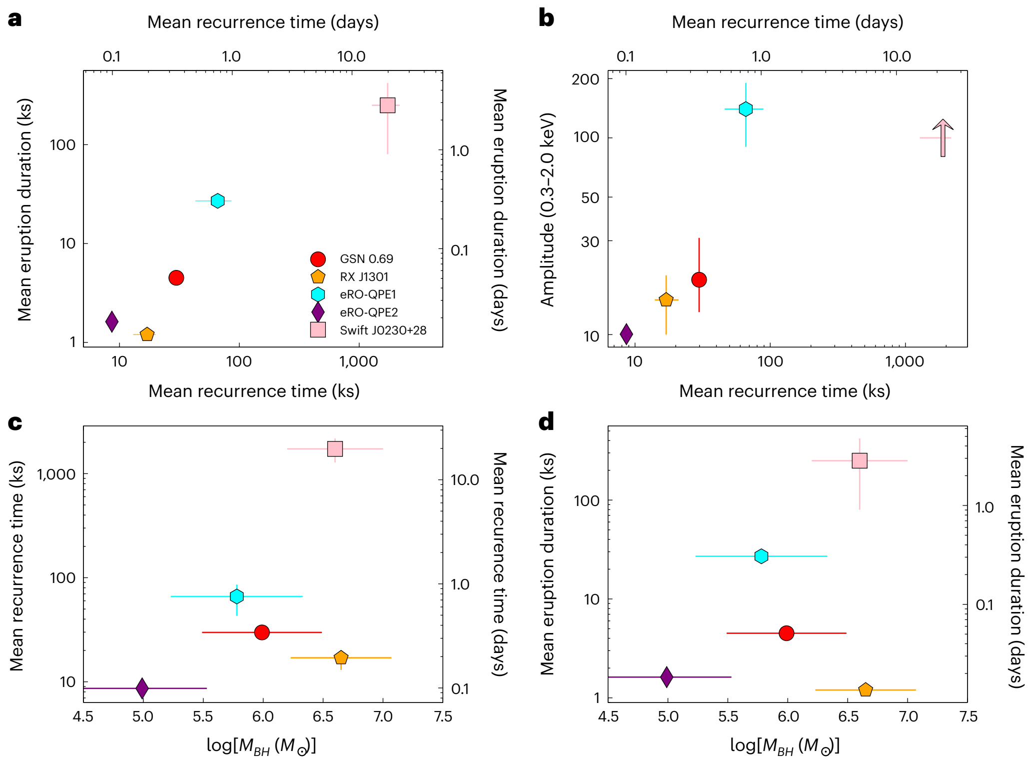

Fig. 5 | Phase space diagrams for QPEs and Swift J0230+28. a, Mean QPE duration versus mean recurrence time. **b**, Amplitude (0.3–2.0 keV band) versus mean recurrence time. **c**, Mean recurrence time versus black hole mass (M_{BH}) derived from host-galaxy stellar velocity dispersion. **d**, Mean eruption duration versus black hole mass (M_{BH}). **a** and **b** show some tentative correlations, which would be extended by at least an order of magnitude if Swift J0230+28 were considered to be a QPE source. There is no correlation between the timing properties and the M_{BH}. This figure is based on ref. 97. The values are shown in Extended Data Table 2. Uncertainties in the timing properties and amplitudes represent the full range of observed values, and the uncertainties in M_{BH} are 1σ.

the strong constraint on Swift J0230+28's host emission before the beginning of the eruptions as well as between eruptions ($\lambda_{\mathrm{Edd}} \leq 0.002$) makes it extremely unlikely that a pre-existent standard thin disk is present, and the lack of any UV or optical variability makes accretion-disk instabilities an unfavourable interpretation for Swift J0230+28's eruptions, given that these models require either one or both of these to be observed (see Supplementary Information, 'Accretion disk instabilities' for details).

The repeated partial tidal disruptions of a star on a bound orbit about a MBH have been proposed to explain both RNTs and QPEs. The repeated partial disruptions of a main sequence star can explain the properties of RNTs[14–18]. For Swift J0230+28, if the X-ray eruptions arise from accretion and the accretion efficiency is of the order of 10%, the mass accreted per eruption would be $\sim10^{-4}$–$10^{-5}\,M_{\odot}$ ('Eruption energetics'). This implies that the mass lost by the star per orbit is a very small fraction of the total stellar mass, which would suggest that the pericentre distance of the star is extremely fine-tuned to coincide with the partial tidal disruption radius[31]. This raises the question of how the star achieved such a fine-tuned distance, given our constraints on the beginning of the eruptions ('Constraints on the start of the eruptions'). Furthermore, the shape of Swift J0230+28's eruptions is the opposite of the fast rise and longer decay expected from fallback accretion. Repeated partial tidal disruptions of a white dwarf, as proposed to explain the hour-long eruptions in QPE sources[32,33], can likely be excluded for Swift J0230+28 given that a standard white dwarf mass and corresponding radius[34] yield a tidal disruption radius that is close to a factor of 10 smaller than the direct capture radius of a $10^{6.6}\,M_{\odot}$ non-spinning black hole (see Supplementary Information, 'Repeating partial tidal disruption event' for details).

After the discovery of the first QPE source, a series of alternative models related to distinct types of EMRIs have been proposed to explain the few-hours to a day, X-ray-only eruptions, which could, in principle, be extended to explain Swift J0230+28. These include a compact object or star colliding with a pre-existing accretion disk or advection-dominated accretion flow[35–37] (Supplementary Information, 'Accretion disk–perturber interaction'), the mass transfer from a single orbiting star undergoing Roche-lobe overflow around the MBH[38,39] (Supplementary Information, 'Stellar mass-transfer'), a pair of interacting stellar EMRIs[40] (Supplementary Information, 'Interacting stellar EMRIs') or the compression of stream clumps from a past TDE[41,42] (Supplementary Information, 'Compressed reformed clumps from a past TDE'). Several of these models can reproduce Swift J0230+28's features, although they also suffer from inherent modelling uncertainties, degeneracies or finely tuned parameters, as we discuss in detail in Supplementary Information, 'Extreme mass ratio inspirals (EMRIs)'. Accurately constraining the characteristics of the physical system operating in Swift J0230+28 thus remains a challenge.

Although the physical origin of QPEs, RNTs and now Swift J0230+28 are still the subject of debate, their discovery inaugurates a new and exciting perspective on the study of transient events associated with MBHs, and Swift J0230+28 has demonstrated the existence of a new timescale associated with these phenomena. In particular, if Swift J0230+28 is a member of the same family as the four known QPE sources—despite their slightly distinct properties—and those originate from the same type of physical system, then the physical system's period needs to be scalable from a few hours to several days, that is, more than two orders of magnitude, which would pose a strong constraint on potential theoretical models. Furthermore, a growing body of literature suggests that these QPEs are electromagnetic counterparts of EMRIs, with important implications for the future of multimessenger astrophysics.

The serendipitous discovery of Swift J0230+28 also highlights exciting astrophysics that we are currently missing due to the lack of wide-field and time-domain X-ray surveys. The eROSITA instrument[43] on the Spectrum-Roentgen-Gamma space observatory[44] has made progress in the field; however, its multiple visits of a field separated by 4 h that are only revisited every 6 months makes it extremely unlikely to discover transients that vary on day timescales, such as Swift J0230+28. In the near future, with its combination of a wide field of view and high cadence, the Einstein Probe[45] should, in principle, be able to discover more events like Swift J0230+28, although its shallow sensitivity combined with the likely very low rate of such events may result in no such discoveries. Only a deep and wide-field time-domain X-ray mission would be able to systematically discover a population of Swift J0230+28-like objects.

Methods

Observations and data analysis

This work is based on new data acquired by five different telescopes and instruments and also archived data, across the entire electromagnetic spectrum (namely radio, IR, optical, UV and X-rays). Below, we describe the data and their relevant reduction and analysis procedures. Throughout this paper, we adopt a standard Λ cold dark matter cosmology with Hubble constant, matter density parameter and dark energy density parameter, respectively equal to $H_0 = 67.4$ km s^{-1} Mpc^{-1}, $\Omega_m = 0.315$ and $\Omega_\Lambda = 1 - \Omega_m = 0.685$ (ref. 46). Using the Cosmology Calculator[47], Swift J0230+28's redshift (z) of 0.036 corresponds to a luminosity distance of 165 Mpcs.

Swift XRT. The field containing the position of Swift J0230+28 was observed by Swift between December 2021 and January 2022 following the discovery of the supernova SN2021afkk located 4.25 arcmin from the position of Swift J0230+28. During that time, X-rays were not detected from the position of Swift J0230+28 with a 0.3–2 keV flux upper limit of 2×10^{-14} erg s^{-1} cm^{-2}. After a gap of 164 days, Swift again started monitoring the field of view on 22 June 2022, making the first detection of the new X-ray source at the position with right ascension 37.57140° and declination 28.60124° with an uncertainty of 3.4" (radius, 90% confidence). Although monitoring continues at the time of writing of this manuscript, we include all data taken until 8 February 2023 (MJD 59,983).

We started the XRT data analysis by downloading the data from the HEASARC public archive. We extracted the cleaned event files by running the xrtpipeline on each observation ID. For each such ID, we ran a detection pipeline[48], using a circular extraction region centred on (02:30:17.1, +28:36:04.5) (J2000.0 epoch) with a radius of 47" and a background using an annulus centred on the source position with inner and outer radii of 80" and 250", respectively. For a source to be considered as a detection, we required that it was detected above the background at a confidence of at least 3σ in a Bayesian framework[49]. Below that, we considered it to be a non-detection.

XRT count rate to flux and luminosity conversion. We followed the procedure below to convert from the observed 0.3–2.0 keV background-subtracted count rate to the observed 0.3–2.0 keV flux and luminosity.

(1) We extracted a combined source spectrum using observation IDs if the source was detected above 3σ.
(2) We combined the corresponding individual exposure maps and used the result to compute a combined ancillary response file by following the steps outlined on XRT's data analysis webpages: https://www.swift.ac.uk/analysis/xrt/exposuremaps.php and https://www.swift.ac.uk/analysis/xrt/arfs.php.
(3) Using ftool ftgroupha, we grouped the spectrum using the optimal binning scheme of ref. 50 with the additional requirement that there were at least 20 counts per spectral bin.
(4) The resulting combined spectrum was then fitted with a thermal model, that is, TBabs × zashift × diskbb in XSPEC. TBabs's column was fixed at the Milky Way value (7.2×10^{20} cm^{-2}) using the HEASARC N_H calculator: https://heasarc.gsfc.nasa.gov/cgi-bin/Tools/w3nh/w3nh.pl. This gave an acceptable χ^2 degrees of freedom of 12/11. The mean 0.3–2.0 keV background-subtracted count rate in this combined spectrum was 1.73×10^{-2}. The observed flux and luminosity were 4.3×10^{-13} erg s^{-1} cm^{-2} and 1.5×10^{42} erg s^{-1}, respectively. Based on this, we derived a scale factor for converting the background-subtracted 0.3–2.0 keV count rate to flux (luminosity) of 2.5×10^{-11} erg s^{-1} cm^{-2} count^{-1} s^{-1} (9×10^{43} erg s^{-1} counts^{-1} s^{-1}).

Estimating the XRT X-ray upper limit. If a source was not detected in several observations taken during the low-flux state between eruptions, then we estimated its flux upper limit as follows:

(1) For n consecutive non-detections (source less than 3σ above background), we extracted a combined 0.3–2.0 keV image for the n observation IDs.
(2) Using ximage's sosta functionality, we estimated the upper limit of the count rate for each group of n non-detections and obtained the upper limit of the 3σ flux using the scaling factor determined in 'XRT count rate to flux and luminosity conversion'. We attributed the combined upper limit of the grouped observations for each observation ID.
(3) We estimated the upper limit of the 0.3–2.0 keV flux for the combined image of all non-detections, which of 7×10^{-4} counts s^{-1} translated to roughly 2×10^{-14} erg s^{-1} cm^{-2}.
(4) We performed a similar procedure for the 2–10 keV band to estimate an upper limit for AGN or corona emission. We obtained 5×10^{-4} counts s^{-1}. Assuming a power-law spectrum with $\Gamma = 2$, this translated to an upper limit of the 2–10 keV flux of 3×10^{-14} erg s^{-1} cm^{-2}.

The resulting XRT light curve showing flux (luminosity) versus time is shown in Fig. 1a. Detections are shown as solid circles with error bars representing 1σ uncertainty. Non-detections are shown as inverse triangles.

Swift/UVOT. All data were processed with heasoft v.6.29c. We used the uvotsource package to extract the photometry measurements made by the ultra-violet optical telescope (UVOT) on Swift using an aperture of 5". We included observations made before and during the X-ray transient. Given that most observations were performed in the 'filter of the day' configuration, data from all UVOT filters are not available for all epochs. Photometry was corrected for Galactic extinction with an extinction color index of $E(B - V) = 0.086$ (ref. 51). There is no statistically significant variability in any of the UVOT filters. We show the well-sampled UV W1 and U filter light curves in Fig. 1c.

NICER. Following Swift/XRT's detection of highly variable X-ray emission from Swift J0230+28, NICER started a monitoring programme as part of the director's discretionary time (DDT). NICER observations started on 23 June 2022 (MJD 59,753) and continue at the time of writing of this paper. Here we include data taken until 1 February 2023 (MJD 59,976). NICER's observing cadence varied during this time. There were one or two exposures per day in the epochs between the eruptions and several exposures per day during the eruptions. The individual exposures varied in length between 200 and 1,000 s. A stacked image from the XRT (~160 ks, see the top left panel Extended Data Fig. 5) shows that only Swift J0230+28 was detected within the NICER field of view, enabling detailed analyses of NICER spectra with no concerns about contamination by other sources.

We started our data analysis by downloading the data from public HEASARC archive (https://heasarc.gsfc.nasa.gov/docs/archive.html).

We essentially followed the same reduction procedures as outlined in detail in refs. 52,53). The cleaned events lists were extracted using the standard NICER data analysis software (HEASoft v.6.29) tasks nicercal, nimpumerge and nicerclean. The latest NICER calibration release xti20221001 (1 October 2022) was used. The cleaned event files were barycentre-corrected using the barycorr ftools task. Swift J0230+28's coordinates (J2000.0): (02:30:17.1, +28:36:04.) were used along with refframe=ICRS and ephem=JPLEPH.430. The good time intervals (GTIs) were extracted with the nimaketime tool using the default filters: nicersaafilt=YES, saafilt=NO, trackfilt=YES, ang dist=0.015, st valid=YES, cor range=‘*-*’, min fpm=38, underonlyrange=0-200, overonlyrange=‘0.0-1.0’, overonly expr=‘1.52*COR SAX**(-0.633)’. Conservative values elv=30 and br earth=40 were used to avoid optical loading by reflected light.

Converting from NICER count rate to luminosity. We computed the fluxes on a per GTI basis using the following procedure:

1. We extracted time-resolved NICER spectra of the source and estimated background spectra using the 3c50 model[54]. Corresponding response files (arf and rmfs) were extracted using the nicerarf and nicerrmf tools.
2. Because the 0.8–1.3 keV band-pass was occasionally dominated by systematic residuals, we fitted each of the above spectra in the 0.3–0.8 keV with a thermal model (tbabs × zashift × diskbb) in XSPEC (ref. 55). Following the recommendation in ref. 54, we considered only spectra for which the background-subtracted source count rate was greater than 0.25 counts s^{-1} and had a signal-to-noise (S/N) ratio (source background-subtracted over background) higher than 3.
3. Using the above spectral fitting, we estimated an epoch-dependent background-subtracted 0.3–0.8 keV count rate to observed luminosity conversion factor, which was used to compute the observed luminosities for each GTI. All GTIs with a background-subtracted 0.3–0.8 keV count rate of less than 0.25 count s^{-1} or S/N ratio less than 3 were assigned an upper limit for the 0.3–0.8 keV flux of 1.79×10^{-13} erg s^{-1} cm^{-2} (triangles in Fig. 1b).

For all NICER spectral fitting in this work, we used an optimal spectral binning scheme[50], χ^2 statistics and an additional 1.5% systematic uncertainty. As for the Swift/XRT fitting, we always assumed that the Galactic absorption followed HEASARC's N_H calculator.

Very Large Array. We observed Swift J0230+28 with the Karl G. Jansky Very Large Array (VLA), National Science Foundation (NSF), on 2 July 2022 (MJD 59,762), 20 September 2022 (MJD 59,842) and 20 December 2022 (MJD 59,933). The VLA was in its highest-resolution A configuration during the first observation, its lowest-resolution D configuration during the second and the intermediate C configuration during the third. All observations had 1 h of exposure time and were conducted at a mean frequency of 10 GHz. The data were reduced in CASA[56] using standard procedures. We additionally performed amplitude and phase self-calibration on the September data. There was no detection at the position of the source in the first and third observations, with 3σ upper limits of 15 and 25 μJy, respectively. However, in our second observation on 20 September 2022, we detected an unresolved radio source with a flux density of 93 ± 7 μJy (13σ detection).

Optical spectra. Keck II/ESI. On 24 October 2022, we obtained a medium-resolution spectrum of the host-galaxy nucleus using the echellette spectrograph and imager (ESI)[57] on the Keck II telescope. We used the echelle mode and a slit width of 0.5", which gives an instrumental broadening of $\sigma_{\rm inst} = 15.8$ km s^{-1}. The exposure time was 15 min. The median S/N from 4,500 to 5,600 Å was 9.

VLT/X-shooter. The host galaxy was also observed under DDT programme 110.2599 on 17 November 2022 with X-shooter[58] mounted on the Unit Telescope 3 (Melipal) of the Very Large Telescope (VLT). Slit widths of 1/0.9/0.9 arcsec were used for the UVB/visible/near-IR arms, respectively, providing a spectral resolution R = 5,400/8,900/5,600 and covering the spectral range 3,500–24,800 Å. Exposure times were 2 × 1,497/1,411/1,200 s in the UVB/visible/near-IR arms, with an on-slit nod to facilitate sky line subtraction in the near-IR arm. We reduced the data using the standard pipeline recipes within esoreflex. For the UVB and visible arms, we used recipes for stare observations to increase the S/N. Strong, extended nebular emission from the host galaxy complicates the sky subtraction, as it leaves strong residuals and oversubtractions, especially in the Balmer lines. To measure the line profiles and fluxes for the diagnostic diagrams, we, therefore, used extractions without subtracting the skylines. If the emission lines were masked, then to measure the velocity dispersion, we used sky-subtracted extractions. Continuum-normalized spectra for the Hβ + [O III] and Hα + [N II] bands are shown in the bottom panel of Extended Data Fig. 5.

Continuum and emission-line fitting. We measured the velocity dispersion σ_* with the penalized pixel-fitting (pPXF) software[59,60], which fits an absorption line spectrum by convolving a template stellar spectral library with Gauss-Hermite functions. We used the ELODIE v.3.1 high-resolution (R = 42,000) library[61,62] and masked wavelength ranges of common galaxy emission lines, hydrogen Balmer lines, telluric regions and an instrument artefact feature at an observer-frame wavelength of ~4,510 Å. Following previous works[63–66], we performed 1,000 Monte Carlo simulations to robustly determine σ_*.

The Keck spectrum has a relatively low S/N ratio (a factor of 2 smaller than that of the X-shooter data) and covers a limited wavelength range (4,500–5,600 Å compared to 3,500–9,000 Å for X-shooter). Both of these factors can introduce systematic uncertainties related to template mismatching and spurious results in the Markov chain Monte Carlo step. For these reasons, we used the X-shooter data to measure the velocity dispersion and estimate the black hole mass.

We measured a velocity dispersion of $\sigma_* = 87 \pm 2$ km s^{-1}, which along with the $M_{\rm BH}$ versus σ relation[12] allowed us to estimate a black hole mass of $\log M_{\rm BH} = 6.6 \pm 0.4\, M_\odot$.

Emission and absorption line fluxes and equivalent widths (EWs) were measured using continuum-normalized versions of the ESI and X-shooter spectra. We included a low-order polynomial for the continuum and single Gaussian components for each emission line, including Hβ, Hα, [O III] λ5,007, [O I] λ6,300, and the [N II] and [S II] doublets. No broad emission-line components were evident. Typical linewidths for the narrow components were 150–200 km s^{-1}. Some lines show weak asymmetries (where the lines are skewed to the blue wing). The line measurements and their ratios were used to locate the host-galaxy nucleus on diagnostic Baldwin, Phillips and Telervich (BPT) and $W_{\rm H\alpha}$ versus [N II]/Hα (WHAN) diagrams, as shown in the top and lower left panels of Extended Data Fig. 6. From the X-shooter spectrum, we also measured the Hδ Lick absorption index[67], which can be used to identify quiescent Balmer strong and E+A (postmerger) galaxies. We plotted Swift J0230+28 among the Sloan Digital Sky Survey population (grey background points) and included measurements from the TDE sample from the Zwicky Transient Facility[68] and QPE host galaxies[69] in the bottom right panel of Extended Data Fig. 6. Swift J0230+28 is classified as a quiescent Balmer strong galaxy. Such galaxies comprise less than 2.3% of the total galaxy population. This is consistent with the over-representation observed in the QPE host population[69].

Time-resolved X-ray analyses

X-ray light curve. Swift J0230+28 showed phases of high (detection) and low (non-detections) activity over the course of our Swift/XRT monitoring (Fig. 1). A quick visual inspection suggests that these eruptions repeated roughly every 3 weeks. To test for quasi-periodicity, we extracted a Lomb–Scargle periodogram (LSP) of the Swift/XRT 0.3–2.0 keV light curve following the description in refs. 10,11, which is shown in Fig. 2. Not surprisingly, the LSP shows two consecutive bin peaks around 21–23 days, with the bin with highest power at 21.8 days. The FWHM of the two bins combined resulted in a peak period of $21.8^{1.2}_{-0.5}$ days. Therefore, the LSP confirms the quasi-periodic nature of Swift J0230+28's eruptions.

The eruptions of Swift J0230+28 are apparently asymmetric, with slower rises than decays. To quantify such asymmetries, we fitted the six best-sampled eruptions, namely around E3, E4, E5, E6, E10 and E11, with an asymmetric Gaussian function $G(\mu, \sigma_+, \sigma_-)$ (ref. 70), where $\sigma_\pm$ are the equivalent positive/negative σ. We used either the NICER or the Swift light curve depending on which had a better sampling of the eruption's shape at the given epoch. In the lower left-hand panel of Extended Data Fig. 5 we show the best-fitting asymmetric Gaussian to the six eruptions. In the right panel, we quantify the asymmetry in the eruptions by plotting the σ_+/σ_- ratios, which vary between 0.60 ± 0.10 and 0.90 ± 0.05 and have a median of $\langle\sigma_+/\sigma_-\rangle \approx 0.7$, thus confirming that the eruptions were asymmetric with slightly slower rises than decays. The best-fitting parameters for the profile are shown in Supplementary Table 1.

X-ray spectra. The high count rate resulting from the high effective area of NICER allowed us to make detailed time-resolved spectral analyses, which are not possible with the Swift/XRT data. First, we stacked the NICER data for the detected epochs in bins of ~1 day, each spectrum or bin having between 300 and 9,000 counts. The energy range in which the source was detected above the background varied depending on the phase of the eruption; however, for all epochs, the source was detected at least up to 0.8 keV. Hence, to measure the luminosities and temperatures, we performed the fitting procedures described in 'Converting from NICER count rate to luminosity' in the 0.3–0.8 keV band. The temperature varied by a factor of two, whereas the luminosity (in the 0.3–0.8 keV band) varied by a factor of 10 between 5×10^{41} and 5×10^{42} erg s^{-1}.

The resulting values are shown in Extended Data Table 2. The evolution of temperature as a function of time is shown in the left-hand panel of Fig. 4. The vertical dashed lines show the peak of each eruption (as fitted in 'X-ray light curve'). At each eruption, the temperature started at ~100 eV and continuously increased up to ~200 eV during the decay. Interestingly, the temperature did not peak at the luminosity peak but instead during the decay. Despite the absence of a clear hotter when brighter trend in the temperature evolution, we employed the linmix package[71] to fit the relationship between the two parameters and still found a positive correlation in the form of $L \propto T_{\rm in}^{1.9\pm0.5}$, although the large scatter is likely driven by the hotter temperatures in the decay phases.

To increase the S/N ratio and probe the spectra shape at energies higher than 0.8 keV, we divided each of the four eruptions probed by NICER (namely, those around E4, E5, E6 and E10) into three phases (rise, peak and decay) and produced a stacked spectrum for each. The resulting spectra have background-free counts of between ~2,000 and ~20,000 and were detected above the background at higher energies, up to 1.4 keV for some peak and decay spectra. We fitted the resulting high-S/N-ratio spectra assuming the same model as before (TBabs × zashift × diskbb), which resulted in the χ^2 degrees of freedom varying between ~1.1 and ~2.5, with residuals present both at the softest end of the spectra and around 1.0 keV for some peak and rise spectra. We then added an intrinsic absorption component at the redshift of the source (TBabs × zTBabs × zashift × diskbb). This absorption takes care of the residuals at the softer energies and results in better fitting for all spectra, with χ^2 degrees of freedom between ~0.9 and ~1.9. The best-fitting intrinsic column density was $N_{\rm H} \approx (1–3) \times 10^{20}$ cm^{-2} in all spectra.

We show the stacked spectra and best-fitting model in Fig. 3. The respective residuals are shown in Extended Data Fig. 3. For a few of the spectra, for example some of the peak phases, there are absorption-like residuals around 1.0 keV. For others, for example some of the decay spectra, the residuals are randomly distributed. A detailed study of whether such residuals are intrinsic to the source, for example an absorption line like the one detected for TDE ASASSN-14li (ref. 72), or are merely an instrumental or systematic residual from the NICER instrument is beyond the scope of this study. If the former is confirmed, the results will be presented in a separate study.

We also tested alternative models to the continuum. Changing diskbb for a phenomenological power law or a single-temperature black body resulted in a worse fit. A thermal bremsstrahlung model (bremss), however, resulted in just a slightly worse fit compared to diskbb, in terms of χ^2 degrees of freedom, for some of the spectra. It had similar fitting statistics in others. For the bremsstrahlung model, the ratio between the best-fitting plasma temperature ($T_{\rm p}$) and the inner disk temperature ($T_{\rm in}$) was consistently $T_{\rm p}/T_{\rm in} \approx 2$, that is $T_{\rm p}$ varied between ~200 and ~400 eV. Moreover, the same relation with the luminosity was observed. We also attempted to fit a model with two continuum components by adding a power law to the thermal emission (TBabs × xzTBabs × zashift × (diskbb + powerlaw)). However, this did not improve the fit quality. In most cases, the best-fitting power-law normalization was negligible. The best overall fit was achieved with TBabs × zTBabs × zashift × diskbb, which is our final model for Swift J0230+28. Extended Data Table 1 lists the best-fitting parameters for the stacked spectra.

Eruption energetics. We estimated the energy released by individual eruptions by integrating their Swift/XRT light curves. An order-of-magnitude estimate resulted in approximately a few $\times 10^{48}$ erg per eruption depending on the duration and amplitude of the eruption. Assuming a 10% efficiency ($\alpha = 0.1$) in the mass to energy conversion and assuming that the eruptions were powered by accretion results in a few $\times 10^{-5}\,M_\odot$ accreted per eruption. If the eruptions started somewhere after 8 January 2022 (MJD 59,587; 'Constraints on the start of the eruptions') then the maximum total mass accreted would have been $<10^{-3}\,M_\odot$.

UV/optical and radio counterparts

Our three VLA observations show two non-detections and one detection. The radio detection coincided with the rise of the E5 eruption, whereas the non-detections coincided with the X-ray quiescent epochs, one between E1 and E2 and the other between E9 and E10, as can be seen in Fig. 1. The three radio images are shown in Extended Data Fig. 4.

The Swift/UVOT data show no variability that is more significant than the 2σ from the level of the pre-eruption host galaxy, as can be seen in Fig. 1. From the observations, we can compute an upper limit for the UV and optical variability. UV W1, in particular, gives the deepest constraint. The derived observed upper limit νL_ν(UV W1) $\leq 1.8 \times 10^{42}$ erg s^{-1}. In TDE studies, the UV/optical integrated emission ($L_{\rm BB}$) is estimated from the fit of a black-body function to the UV/optical broadband spectral energy distribution (SED). The UV/optical to X-ray luminosity ratio ($L_{\rm BB}/L_{\rm X}$) is the parameter of interest when studying the shape of the SED. Assuming a typical temperature found in the UV/optical component of TDEs, namely around 20,000 K (ref. 68), the UV W1 upper limit translates to $L_{\rm BB} \leq 3 \times 10^{42}$ erg s^{-1}. This means that at the peak of the X-ray eruptions, $L_{\rm BB}/L_{\rm X} \leq 0.5$. From the fitting of the stacked spectra ('Time-resolved X-ray analyses'), we found evidence for a very small intrinsic column density at the maximum ~3×10^{20} cm^{-2}, assuming a standard gas-to-dust ratio ($N_{\rm H} = 5 \times 10^{21}$ cm$^{-2} \times E(B-V)$)[73], which translates to a maximum dust extinction of $E(B-V) \approx 0.06$. Assuming a standard extinction law[74], the intrinsic extinction-corrected emission in the UV W1 band could be at most a factor of ~40% higher. This just slightly increases the upper limits for the UV W1 and integrated UV/optical emission to νL_ν(UV W1) $\leq 2.6 \times 10^{42}$ erg s^{-1} and $L_{\rm BB} \leq 4.2 \times 10^{42}$ erg s^{-1}, respectively, meaning that extinction cannot be the cause of the UV/optical faintness. Thus, this faintness is an intrinsic characteristic of Swift J0230+28 eruptions.

The host galaxy

The position derived from XRT data for Swift J0230+28 is 0.2" away from the photometric centre of the nearby spiral galaxy 2MASX J02301709+2836050, which is located at 165 Mpcs. The galaxy has prominent blue spiral arms and a redder bright nuclear core (see the top right panel in Extended Data Fig. 5).

The host galaxy does not appear in large AGN catalogues[75,76]. There is no previous X-ray detection at the position of this galaxy: the X-ray upper limit server[77] returns only upper limits from the XMM-Newton Slew Survey, ROSAT All-sky Survey and previous observations by Swift/XRT (see exact values in 'Constraints on the start of the eruptions'). The galaxy shows no excess in the IR bands that could indicate the presence of a torus emitting hot dust. The Wide-field Infrared Survey Explorer (WISE)[78] IR W1 − W2 colour ≈ 0.1 does not pass standard AGN selection criteria[79]. Instead, it is consistent with emission from a pure stellar population. The NeoWISE[80] light curves from 2014 to 2021 show no significant variability ($<1\sigma$). Our recently obtained optical spectra show no signs of broad emission lines. Together, these multiwavelength properties exclude the existence of a bright AGN (for example, Seyfert I or quasar-like) in Swift J0230+28's host.

The narrow emission lines in the ESI and X-shooter spectra can be used to locate the host-galaxy nucleus on diagnostic BPT[81] and WHAN[82] diagrams and to investigate the ionization mechanism producing the lines, as shown in the top and bottom panels of Extended Data Fig. 6. Swift J0230+28's host is above the theoretical upper limit for pure star-forming galaxies[83] (meaning that an additional ionizing mechanism is necessary to produce these line ratios) and around the empirical separation between Seyfert and low-ionization nuclear emission-line region[84,85] on both [N II] and [S II] diagrams. The WHAN diagram[82] can be used to classify the nucleus further: the low EW Hα results in classification as a weak AGN. In general, the multiwavelength properties agree that Swift J0230+28's may host (or have hosted) a LLAGN. We gathered archival photometric data on the host galaxy: in the UV and optical from UVOT ('Swift/UVOT'), in the optical and near IR (g, r, i, z and y bands) from the PAN-STARRS survey[86], near IR (K, H and J bands) from the 2MASS survey[87] and in the mid-IR (W1, W2, W3 and W4 bands) from the WISE survey[88]. When gathering all the photometric data, we used the values extracted from aperture sizes as close to the Kron radius (12') as possible for all the surveys. To estimate the host-galaxy properties, we modelled the resulting SED using the flexible stellar population synthesis module[89]. We used the Prospector software[90] to run a Markov chain Monte Carlo sampler[91]. We assumed an exponentially decaying star formation history and a flat prior on the five free model parameters: stellar mass ($M_\star$), stellar metallicity (Z), $E(B-V)$ extinction (assuming the extinction law from ref. 74), stellar population age (t_{age}) and the e-folding time of the exponential decay of the star formation history (τ_{sfh}).

The observed and modelled SEDs are shown in Extended Data Fig. 7, which also shows the best-fitting parameters and their uncertainties. Of particular interest is the total stellar mass ($M_* \approx 2\times10^{10}\,M_\odot$), which can be used to obtain an order-of-magnitude estimate of M_{BH}. Using the M_* versus M_{BH} relation[13], we obtain $\log(M_{\mathrm{BH}}/M_\odot) = 6.9 \pm 0.7$, where the uncertainty accounts for both the statistical and the spread of the scaling relation, although it is dominated by the former. The resulting M_{BH} value is consistent, within the error bar, with the one obtained from the σ_* versus M_{BH} relation. We adopted the value obtained from σ_*, given the smaller spread and systematically more consistent values obtained from σ_* versus M_{BH} (refs. 13,92).

Using a bolometric correction[93] and the measured extinction-corrected [O III] λ5,007 Å luminosity of $\sim5\times10^{38}$ erg s^{-1}, we estimated the upper limit of the bolometric luminosity of this LLAGN to be $L_{\mathrm{quiet,bol}} \le 2\times10^{42}$ erg s^{-1}. From the 2.0–10.0 keV luminosity upper limit ($\sim9\times10^{40}$ erg s^{-1}; 'Estimating the XRT X-ray upper limit') and the bolometric correction in ref. 94, we also estimated an upper limit of $L_{\mathrm{quiet,bol}} \le 9\times10^{41}$ erg s^{-1}. Given that the value derived from [O III] represents the mean accretion rate in the last few million years (which represents the time to ionize the entire narrow line region), that star formation likely contributes to a considerable fraction of its luminosity and that the hard X-rays (2.0–10.0 keV) give a more precise estimate of the current accretion state, we adopted 9×10^{41} erg s^{-1} as our estimate of the upper limit for the bolometric luminosity of the LLAGN in Swift J0230+28's host. Combined, the measured $L_{\mathrm{quiet,bol}}$ and M_{BH} result in an Eddington ratio $\lambda_{\mathrm{Edd}} = L_{\mathrm{bol}}/L_{\mathrm{Edd}} < 0.002$, confirming the extremely low accretion rate of Swift J0230+28's host galaxy before the eruptions.

Constraints on the start of the eruptions

We searched for archival X-ray observations at Swift J0230+28's position to constrain the start of the eruptions. There have been no previous X-ray detections at this position. The X-ray upper limit server[77] returns a 0.2–2.0 keV flux $\le3.3\times10^{-13}$ from a ~330 s observation by the ROSAT All-sky Survey in 1990 (ref. 95) and $\le5.2\times10^{-13}$ erg s^{-1} cm^{-2} from a ~9 s exposure by the XMM-Newton Slew Survey in 2005 (ref. 96). The field containing the position of Swift J0230+28 was observed by XRT between 1 and 11 December 2021 with a 3 day cadence and between 24 December 2021 and 8 January 2022, also at a 3 day cadence. There were no detections during this early monitoring, and all the upper limits were below the flux level of the first detection. The non-detections during this early XRT monitoring put a hard constraint on the start of the QPEs, as it is unlikely that no eruptions would be detected during high-cadence month-long monitoring if they had already started. To quantify this likelihood, we performed the following series of simulations:

- We shifted the exactly known XRT light curve (shown in Fig. 1 for MJD 59,752–59,983) to the epochs of the early XRT monitoring (shown in red in Extended Data Fig. 1) while maintaining its cadence and gaps.
- We checked to see if at least one of the early-time observations matched a detection of the simulated light curve, given a ±0.5 day range.
- We repeated the process 10,000 times but randomly changed the relative shift between the simulated light curve and the early monitoring observations in each iteration while ensuring the epochs of the simulated light curves included the epochs of the early monitoring.
- We checked to see how many of these 10,000 simulations have at least one detection.

From the simulations, we found that 88% of the time, we would have made at least one detection if the known light curve (series of eruptions) were present during the early monitoring. This means that the probability of not observing such eruptions in the early monitoring is only 12%. However, we note that this is driven mainly by the large period without long-lived (several days long) eruptions between MJD 59,880 and MJD 59,940. If the simulated light curve had only the six first consecutive long eruptions (from discovery up to MJD 59,880), then the probability of making no detections during the early monitoring would drop to 0.1%. Therefore, we can conclude that the eruptions in Swift J0230+28 most likely started between the end of the early monitoring campaign and the date of the first detection (that is between 8 January and 22 June 2022). In Extended Data Fig. 1, we show the long-term light curve with all the archived non-detections as a function of time.

Data availability

All the NICER and Swift data presented here are public and can be found in the NASA archives at the following URL: https://heasarc.gsfc.nasa.gov/cgi-bin/W3Browse/w3browse.pl. The VLA data are available from the archives of the National Radio Astronomy Observatory at https://data.nrao.edu/portal/#/. X-shooter spectra will be available from the ESO archive after the 12 months' proprietary period has passed. Keck/ESI data can be shared by a request to the corresponding authors.

The general relativistic magnetohydrodynamic simulation data, described in Supplementary Information, 'Accretion disk–perturber interaction', are available by a request to the corresponding author. The data underlying the multiwavelength light curves presented in Fig. 1 are available at https://zenodo.org/records/10238766.

References

1. Chen, T. W. et al. ATLAS21bmvp (AT 2021afkk): discovery of a fast rising candidate supernova in UGC01971 (60 Mpc). *Transient Name Serv. AstroNote* **300**, 1–300 (2021).
2. Evans, P. A. et al. A real-time transient detector and the living Swift-XRT point source catalogue. *Mon. Not. R. Astron. Soc.* **518**, 174–184 (2023).
3. Evans, P. A. et al. Monthly quasi-periodic eruptions from repeated stellar disruption by a massive black hole. *Nat. Astron.* **7**, 1368–1375 (2023).
4. Evans, P. A., Campana, S. & Page, K. L. Swift J023017.0+283603: a possible tidal disruption event. *Astron. Telegr.* **15454**, 1 (2022).
5. Evans, P. A., Breeveld, A. A. & Oates, S. R. Further Swift observations of the TDE candidate Swift J023017.0+283603. *Astron. Telegr.* **15461**, 1 (2022).
6. Rees, M. J. Tidal disruption of stars by black holes of 10^6–10^8 solar masses in nearby galaxies. *Nature* **333**, 523–528 (1988).
7. van Velzen, S. et al. Seventeen tidal disruption events from the first half of ZTF survey observations: entering a new era of population studies. *Astrophys. J.* **908**, 4 (2021).
8. Hammerstein, E. et al. The final season reimagined: 30 tidal disruption events from the ZTF-I survey. *Astrophys. J.* **942**, 9 (2023).
9. Guolo, M. et al. A systematic analysis of the X-ray emission in optically selected tidal disruption events: observational evidence for the unification of the optically and X-ray selected populations. Preprint at *arXiv* https://doi.org/10.48550/arXiv.2308.13019 (2023).
10. Scargle, J. D. Studies in astronomical time series analysis. II. Statistical aspects of spectral analysis of unevenly spaced data. *Astrophys. J.* **263**, 835–853 (1982).
11. Horne, J. H. & Baliunas, S. L. A prescription for period analysis of unevenly sampled time series. *Astrophys. J.* **302**, 757 (1986).
12. Gültekin, K. et al. The M–σ and M–L relations in galactic bulges, and determinations of their intrinsic scatter. *Astrophys. J.* **698**, 198–221 (2009).
13. Greene, J. E., Strader, J. & Ho, L. C. Intermediate-mass black holes. *Annu. Rev. Astron. Astrophys.* **58**, 257–312 (2020).
14. Payne, A. V. et al. ASASSN-14ko is a periodic nuclear transient in ESO 253-G003. *Astrophys. J.* **910**, 125 (2021).
15. Liu, Z. et al. Deciphering the extreme X-ray variability of the nuclear transient eRASSt J045650.3−203750. A likely repeating partial tidal disruption event. *Astron. Astrophys.* **669**, A75 (2023).
16. Wevers, T. et al. Live to die another day: the rebrightening of AT 2018fyk as a repeating partial tidal disruption event. *Astrophys. J. Lett.* **942**, L33 (2023).
17. Cufari, M., Coughlin, E. R. & Nixon, C. J. Using the Hills mechanism to generate repeating partial tidal disruption events and ASASSN-14ko. *Astrophys. J. Lett.* **929**, L20 (2022).
18. Liu, C. et al. Tidal disruption events from eccentric orbits and lessons learned from the noteworthy ASASSN-14ko. *Astrophys. J.* **944**, 184 (2023).
19. Miniutti, G. et al. Nine-hour X-ray quasi-periodic eruptions from a low-mass black hole galactic nucleus. *Nature* **573**, 381–384 (2019).
20. Giustini, M., Miniutti, G. & Saxton, R. D. X-ray quasi-periodic eruptions from the galactic nucleus of RX J1301.9+2747. *Astron. Astrophys.* **636**, L2 (2020).
21. Arcodia, R. et al. X-ray quasi-periodic eruptions from two previously quiescent galaxies. *Nature* **592**, 704–707 (2021).
22. Bardeen, J. M. & Petterson, J. A. The Lense–Thirring effect and accretion disks around Kerr black holes. *Astrophys. J. Lett.* **195**, L65 (1975).
23. Nixon, C., King, A., Price, D. & Frank, J. Tearing up the disk: how black holes accrete. *Astrophys. J. Lett.* **757**, L24 (2012).
24. Musoke, G., Liska, M., Porth, O., van der Klis, M. & Ingram, A. Disc tearing leads to low and high frequency quasi-periodic oscillations in a GRMHD simulation of a thin accretion disc. *Mon. Not. R. Astron. Soc.* **518**, 1656–1671 (2023).
25. Liska, M. T. P., Kaaz, N., Musoke, G., Tchekhovskoy, A. & Porth, O. Radiation transport two-temperature GRMHD simulations of warped accretion disks. *Astrophys. J. Lett.* **944**, L48 (2023).
26. Meyer, F. & Meyer-Hofmeister, E. On the elusive cause of cataclysmic variable outbursts. *Astron. Astrophys.* **104**, L10–L12 (1981).
27. Sniegowska, M., Czerny, B., Bon, E. & Bon, N. Possible mechanism for multiple changing-look phenomena in active galactic nuclei. *Astron. Astrophys.* **641**, A167 (2020).
28. Śniegowska, M., Grzkedzielski, M., Czerny, B. & Janiuk, A. Modified models of radiation pressure instability in application to 10, 10^5, and $10^7 M_{\odot}$ accreting black holes. *Astron. Astrophys.* **672**, A19 (2023).
29. Pan, X., Li, S.-L., Cao, X., Miniutti, G. & Gu, M. A disk instability model for the quasi-periodic eruptions of GSN 069. *Astrophys. J. Lett.* **928**, L18 (2022).
30. Kaur, K., Stone, N. C. & Gilbaum, S. Magnetically dominated discs in tidal disruption events and quasi-periodic eruptions. *Mon. Not. R. Astron. Soc.* **524**, 1269–1290 (2023).
31. Guillochon, J. & Ramirez-Ruiz, E. Hydrodynamical simulations to determine the feeding rate of black holes by the tidal disruption of stars: the importance of the impact parameter and stellar structure. *Astrophys. J.* **767**, 25 (2013).
32. Zalamea, I., Menou, K. & Beloborodov, A. M. White dwarfs stripped by massive black holes: sources of coincident gravitational and electromagnetic radiation. *Mon. Not. R. Astron. Soc.* **409**, L25–L29 (2010).
33. King, A. GSN 069 – A tidal disruption near miss. *Mon. Not. R. Astron. Soc.* **493**, L120–L123 (2020).
34. Nauenberg, M. Analytic approximations to the mass–radius relation and energy of zero-temperature stars. *Astrophys. J.* **175**, 417 (1972).
35. Suková, P., Zajaček, M., Witzany, V. & Karas, V. Stellar transits across a magnetized accretion torus as a mechanism for plasmoid ejection. *Astrophys. J.* **917**, 43 (2021).
36. Linial, I. & Metzger, B. D. EMRI + TDE = QPE: periodic X-ray flares from star–disk collisions in galactic nuclei. *Astrophys. J.* https://doi.org/10.3847/1538-4357/acf65b (2023).
37. Lu, W. & Quataert, E. Quasi-periodic eruptions from mildly eccentric unstable mass transfer in galactic nuclei. *Mon. Not. R. Astron. Soc.* **524**, 6247–6266 (2023).
38. Krolik, J. H. & Linial, I. Quasiperiodic erupters: a stellar mass-transfer model for the radiation. *Astrophys. J.* **941**, 24 (2022).
39. Linial, I. & Sari, R. Unstable mass transfer from a main-sequence star to a supermassive black hole and quasiperiodic eruptions. *Astrophys. J.* **945**, 86 (2023).
40. Metzger, B. D., Stone, N. C. & Gilbaum, S. Interacting stellar EMRIs as sources of quasi-periodic eruptions in galactic nuclei. *Astrophys. J.* **926**, 101 (2022).
41. Guillochon, J. & Ramirez-Ruiz, E. A dark year for tidal disruption events. *Astrophys. J.* **809**, 166 (2015).
42. Coughlin, E. R. & Nixon, C. J. The gravitational instability of adiabatic filaments. *Astrophys. J. Suppl. Ser.* **247**, 51 (2020).
43. Predehl, P. et al. The eROSITA X-ray telescope on SRG. *Astron. Astrophys.* **647**, A1 (2021).
44. Sunyaev, R. et al. SRG X-ray orbital observatory. Its telescopes and first scientific results. *Astron. Astrophys.* **656**, A132 (2021).
45. Yuan, W., Zhang, C., Chen, Y. & Ling, Z.*The Einstein Probe Mission* (Springer, 2022).

46. Planck Collaboration et al. Planck 2018 results. VI. Cosmological parameters. *Astron. Astrophys.* **641**, A6 (2020).
47. Wright, E. L. A cosmology calculator for the World Wide Web. *Publ. Astron. Soc. Pac.* **118**, 1711–1715 (2006).
48. Evans, P. A. et al. 1SXPS: a deep Swift X-ray telescope point source catalog with light curves and spectra. *Astrophys. J. Suppl. Ser.* **210**, 8 (2014).
49. Kraft, R. P., Burrows, D. N. & Nousek, J. A. Determination of confidence limits for experiments with low numbers of counts. *Astrophys. J.* **374**, 344 (1991).
50. Kaastra, J. S. & Bleeker, J. A. M. Optimal binning of X-ray spectra and response matrix design. *Astron. Astrophys.* **587**, A151 (2016).
51. Schlafly, E. F. & Finkbeiner, D. P. Measuring reddening with Sloan Digital Sky Survey stellar spectra and recalibrating SFD. *Astrophys. J.* **737**, 103 (2011).
52. Pasham, D. R. et al. The birth of a relativistic jet following the disruption of a star by a cosmological black hole. *Nat. Astron.* **7**, 88–104 (2022).
53. Pasham, D. R. et al. Evidence for a compact object in the aftermath of the extragalactic transient AT2018cow. *Nat. Astron.* **6**, 249–258 (2022).
54. Remillard, R. A. et al. An empirical background model for the NICER X-ray timing instrument. *Astron. J.* **163**, 130 (2022).
55. Arnaud, K. A. XSPEC: the first ten years. *Astron. Soc. Pac. Conf. Ser.* **101**, 17–20 (1996).
56. McMullin, J. P., Waters, B., Schiebel, D., Young, W. & Golap, K. CASA architecture and applications. *Astron. Soc. Pac. Conf. Ser.* **376**, 127–130 (2007).
57. Sheinis, A. I. et al. ESI, a new Keck Observatory echellette spectrograph and imager. *Publ. Astron. Soc. Pac.* **114**, 851–865 (2002).
58. Vernet, J. et al. X-shooter, the new wide band intermediate resolution spectrograph at the ESO Very Large Telescope. *Astron. Astrophys.* **536**, A105 (2011).
59. Cappellari, M. & Emsellem, E. Parametric recovery of line-of-sight velocity distributions from absorption-line spectra of galaxies via penalized likelihood. *Publ. Astron. Soc. Pac.* **116**, 138–147 (2004).
60. Cappellari, M. Improving the full spectrum fitting method: accurate convolution with Gauss–Hermite functions. *Mon. Not. R. Astron. Soc.* **466**, 798–811 (2017).
61. Prugniel, P. & Soubiran, C. A database of high and medium-resolution stellar spectra. *Astron. Astrophys.* **369**, 1048–1057 (2001).
62. Prugniel, P., Soubiran, C., Koleva, M. & Le Borgne, D. New release of the ELODIE library: Version 3.1. Preprint at *arXiv* https://doi.org/10.48550/arXiv.astro-ph/0703658 (2007).
63. Wevers, T. et al. Black hole masses of tidal disruption event host galaxies. *Mon. Not. R. Astron. Soc.* **471**, 1694–1708 (2017).
64. Wevers, T. et al. Black hole masses of tidal disruption event host galaxies II. *Mon. Not. R. Astron. Soc.* **487**, 4136–4152 (2019).
65. French, K. D., Wevers, T., Law-Smith, J., Graur, O. & Zabludoff, A. I. The host galaxies of tidal disruption events. *Space Sci. Rev.* **216**, 32 (2020).
66. Yao, Y. et al. The tidal disruption event AT2021ehb: evidence of relativistic disk reflection, and rapid evolution of the disk-corona system. *Astrophys. J.* **937**, 8 (2022).
67. Worthey, G., Faber, S. M., Gonzalez, J. J. & Burstein, D. Old stellar populations. V. Absorption feature indices for the complete Lick/IDS sample of stars. *Astrophys. J. Suppl. Ser.* **94**, 687 (1994).
68. Hammerstein, E. et al. Tidal disruption event hosts are green and centrally concentrated: signatures of a post-merger system. *Astrophys. J. Lett.* **908**, L20 (2021).
69. Wevers, T., Pasham, D. R., Jalan, P., Rakshit, S. & Arcodia, R. Host galaxy properties of quasi-periodically erupting X-ray sources. *Astron. Astrophys.* **659**, L2 (2022).
70. Barlow, R. J. Asymmetric statistical errors. *Stat. Probl. Part. Phys. Astrophys. Cosmol.* https://doi.org/10.1142/9781860948985_0013 (2004).
71. Kelly, B. C. Some aspects of measurement error in linear regression of astronomical sata. *Astrophys. J.* **665**, 1489–1506 (2007).
72. Kara, E., Dai, L., Reynolds, C. S. & Kallman, T. Ultrafast outflow in tidal disruption event ASASSN-14li. *Mon. Not. R. Astron. Soc.* **474**, 3593–3598 (2018).
73. Predehl, P. & Schmitt, J. H. M. M. X-raying the interstellar medium: ROSAT observations of dust scattering halos. *Astron. Astrophys.* **293**, 889–905 (1995).
74. Calzetti, D. et al. The dust content and opacity of actively star-forming galaxies. *Astrophys. J.* **533**, 682–695 (2000).
75. Véron-Cetty, M. P. & Véron, P. A catalogue of quasars and active nuclei: 13th edition. *Astron. Astrophys.* **518**, A10 (2010).
76. Flesch, E. W. The Million Quasars (Milliquas) v7.2 Catalogue, now with VLASS associations. The inclusion of SDSS-DR16Q quasars is detailed. Preprint at *arXiv* https://doi.org/10.48550/arXiv.2105.12985 (2021).
77. Saxton, R. D. et al. HILIGT, upper limit servers. I Overview. *Astron. Comput.* **38**, 100531 (2022).
78. Wright, E. L. et al. The Wide-field Infrared Survey Explorer (WISE): mission description and initial on-orbit performance. *Astron. J.* **140**, 1868–1881 (2010).
79. Stern, D. et al. Mid-infrared selection of active galactic nuclei with the Wide-Field Infrared Survey Explorer. I. Characterizing WISE-selected active galactic nuclei in COSMOS. *Astrophys. J.* **753**, 30 (2012).
80. Mainzer, A. et al. NEOWISE observations of near-Earth objects: preliminary results. *Astrophys. J.* **743**, 156 (2011).
81. Baldwin, J. A., Phillips, M. M. & Terlevich, R. Classification parameters for the emission-line spectra of extragalactic objects. *Publ. Astron. Soc. Pac.* **93**, 5–19 (1981).
82. Cid Fernandes, R., Stasińska, G., Mateus, A. & Vale Asari, N. A comprehensive classification of galaxies in the Sloan Digital Sky Survey: how to tell true from fake AGN? *Mon. Not. R. Astron. Soc.* **413**, 1687–1699 (2011).
83. Kewley, L. J., Dopita, M. A., Sutherland, R. S., Heisler, C. A. & Trevena, J. Theoretical modeling of starburst galaxies. *Astrophys. J.* **556**, 121–140 (2001).
84. Cid Fernandes, R. et al. Alternative diagnostic diagrams and the 'forgotten' population of weak line galaxies in the SDSS. *Mon. Not. R. Astron. Soc.* **403**, 1036–1053 (2010).
85. Kewley, L. J., Groves, B., Kauffmann, G. & Heckman, T. The host galaxies and classification of active galactic nuclei. *Mon. Not. R. Astron. Soc.* **372**, 961–976 (2006).
86. Kaiser, N. et al. Pan-STARRS: a large synoptic survey telescope array. In *Proc. Survey and Other Telescope Technologies and Discoveries* Vol. 4836 (eds Tyson, J. A. & Wolff, S.) 154–164 (Society of Photo-Optical Instrumentation Engineers, 2002).
87. Cutri, R. M. et al. VizieR Online Data Catalog: 2MASS All-Sky Catalog of Point Sources (Cutri+ 2003). *VizieR Online Data Catalog* II/246 (2003).
88. Cutri, R. M. et al. VizieR Online Data Catalog: AllWISE Data Release (Cutri+ 2013). *VizieR Online Data Catalog* II/328 (2013).
89. Conroy, C., Gunn, J. E. & White, M. The propagation of uncertainties in stellar population synthesis modeling. I. The relevance of uncertain aspects of stellar evolution and the initial mass function to the derived physical properties of galaxies. *Astrophys. J.* **699**, 486–506 (2009).
90. Johnson, B. D., Leja, J., Conroy, C. & Speagle, J. S. Stellar population inference with Prospector. *Astrophys. J. Suppl. Ser.* **254**, 22 (2021).

91. Foreman-Mackey, D., Hogg, D. W., Lang, D. & Goodman, J. emcee: the MCMC hammer. *Publ. Astron. Soc. Pac.* **125**, 306 (2013).
92. Kormendy, J. & Ho, L. C. Coevolution (or not) of supermassive black holes and host galaxies. *Annu. Rev. Astron. Astrophys.* **51**, 511–653 (2013).
93. Pennell, A., Runnoe, J. C. & Brotherton, M. S. Updating quasar bolometric luminosity corrections. III. [O III] bolometric corrections. *Mon. Not. R. Astron. Soc.* **468**, 1433–1441 (2017).
94. Duras, F. et al. Universal bolometric corrections for active galactic nuclei over seven luminosity decades. *Astron. Astrophys.* **636**, A73 (2020).
95. Voges, W. et al. The ROSAT all-sky survey bright source catalogue. *Astron. Astrophys.* **349**, 389–405 (1999).
96. Saxton, R. D. et al. The first XMM-Newton slew survey catalogue: XMMSL1. *Astron. Astrophys.* **480**, 611–622 (2008).
97. Chakraborty, J. et al. Possible X-ray quasi-periodic eruptions in a tidal disruption event candidate. *Astrophys. J. Lett.* **921**, L40 (2021).

Acknowledgements

During the refereeing process of this manuscript, Evans et al. 2023 (ref. 3) published a paper presenting a focused investigation of Swift J0230+28. Those authors' dataset does not include our NICER and radio (VLA) data, but their science case and physical interpretation are like ours. M.G. and S.G. are supported in part by NASA (Grant Nos. 80NSS23K0621 and 80NSSC22K0571). D.R.P. was supported by NASA for this work (Grant No. 80NSSC22K0961). D.R.P. and R.R. acknowledge support from NASA (Grant No. 80NSSC19K1287). M.Z. was supported by the Czech Science Foundation through Junior Star Grant No. GM24-10599M. T.W. warmly thanks the Space Telescope Science Institute for its hospitality during part of this work. P.S. has been supported by the Lumina Quaeruntur fellowship of the Czech Academy of Sciences (No. LQ100032102). This work was supported by the Ministry of Education, Youth and Sports of the Czech Republic through e-INFRA CZ (Grant Nos. 90140 and LM2023047 to V.K.). V.W. was supported by Charles University (Research Programme PRIMUS 23/SCI/019). R.A. acknowledges support from NASA through the NASA Einstein Fellowship (Grant No. HF2-51499) as awarded by the Space Telescope Science Institute, which is operated by the Association of Universities for Research in Astronomy, Inc., for NASA (Contract No. NAS5-26555). This work was supported by the Australian government through the Australian Research Council's Discovery Projects funding scheme (Grant No. DP200102471). E.R.C. acknowledges support from the NSF (Grant No. AST-2006684) and from the Oakridge Associated Universities through a Ralph E. Powe Junior Faculty Enhancement Award. E.C.F. is supported by NASA (Award No. 80GSFC21M0002). K.D.A. acknowledges support from the NSF (Grant No. AST-2307668). We recognize and acknowledge the cultural role and reverence that the summit of Mauna Kea has always had within the indigenous Hawaiian community. We are most fortunate to have the opportunity to conduct observations from this mountain. NICER is a 0.2–12 keV X-ray telescope operating on the International Space Station. The NICER mission and portions of the NICER science team activities are funded by NASA. Observations were made with European Southern Observatory (ESO) telescopes at La Silla Paranal Observatory under programme ID 110.2599. The National Radio Astronomy Observatory is a facility of the NSF operated under cooperative agreement by Associated Universities, Inc.

Author contributions

M.G. led the overall project, wrote a large portion of the paper, performed part of the data analyses and was the principal investigator (PI) of the NICER DDT proposals. D.R.P. reduced the NICER data and performed part of the X-ray analyses. M.Z. and E.R.C. led the theoretical and modelling portion of the project and wrote parts of the paper. V.W., P.S. and V.K. contributed to the modelling and theory portion of the paper. T.W. was the PI of the VLT DDT programme and wrote part of the paper. S.v.V., K.D.A. (PI) and J.M.J. are the team leads of the VLA programme. S.v.V. performed the radio data reduction and analyses. R.R., K.G. and E.C.F. performed the NICER observations. S.G., F.T., Y.Y. and R.A. contributed to gathering, analysing and interpreting data as well as writing the paper and discussions.

Competing interests

The authors declare no competing interests.

Additional information

Extended data Extended data are available for this paper at https://doi.org/10.1038/s41550-023-02178-4.

Supplementary information The online version contains supplementary material available at https://doi.org/10.1038/s41550-023-02178-4.

Correspondence and requests for materials should be addressed to Muryel Guolo.

Peer review information *Nature Astronomy* thanks Margherita Giustini and the other, anonymous, reviewer(s) for their contribution to the peer review of this work.

Reprints and permissions information is available at www.nature.com/reprints.

Publisher's note Springer Nature remains neutral with regard to jurisdictional claims in published maps and institutional affiliations.

Springer Nature or its licensor (e.g. a society or other partner) holds exclusive rights to this article under a publishing agreement with the author(s) or other rightsholder(s); author self-archiving of the accepted manuscript version of this article is solely governed by the terms of such publishing agreement and applicable law.

© The Author(s), under exclusive licence to Springer Nature Limited 2024

---

[1]Department of Physics and Astronomy, Johns Hopkins University, Baltimore, MD, USA. [2]Kavli Institute for Astrophysics and Space Research, Massachusetts Institute of Technology, Cambridge, MA, USA. [3]Department of Theoretical physics and Astrophysics, Masaryk University, Brno, Czech Republic. [4]Department of Physics, Syracuse University, Syracuse, NY, USA. [5]Space Telescope Science Institute, Baltimore, MD, USA. [6]Astronomical Institute of the Czech Academy of Sciences, Prague, Czech Republic. [7]European Southern Observatory, Santiago, Chile. [8]Institute of Theoretical Physics, Charles University, Prague, Czech Republic. [9]Physics Department, Tor Vergata University of Rome, Rome, Italy. [10]INAF - Astronomical Observatory of Rome, Rome, Italy. [11]INFN - Roma Tor Vergata, Rome, Italy. [12]Department of Astronomy, University of Maryland, College Park, MD, USA. [13]NASA Goddard Space Flight Center, Greenbelt, MD, USA. [14]Leiden Observatory, Leiden University, Leiden, the Netherlands. [15]Steward Observatory, University of Arizona, Tucson, AZ, USA. [16]Miller Institute for Basic Research in Science, 468 Donner Lab, Berkeley, CA, USA. [17]Department of Astronomy, University of California, Berkeley, CA, USA. [18]International Centre for Radio Astronomy Research - Curtin University, Perth, Western Australia, Australia. [19]Center for Research and Exploration in Space Science and Technology (CRESST), NASA/GSFC, Greenbelt, MD, USA. ✉e-mail: mguolop1@jhu.edu

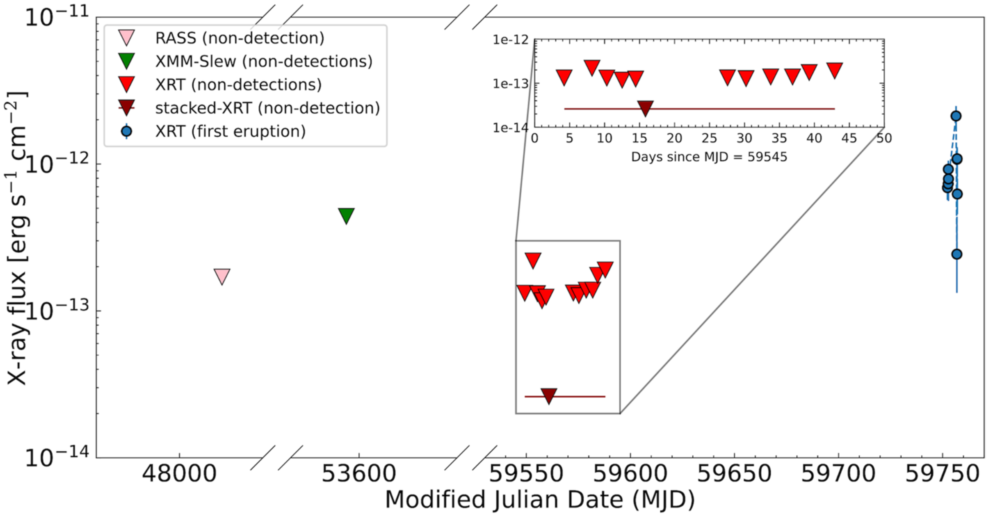

Extended Data Fig. 1 | Constraint on the beginning of the eruptions in Swift J0230+28. Historical X-ray light curve, 3σ upper limits from non-detection in 1990 by RASS (pink triangle), in 2005 by *XMM-Newton*-Slew survey (green triangle) and multiple *Swift*/XRT observations between 1 December 2021 and 8 January 2022 (red triangles). The multiple consecutive non-detections of XRT constrain that the eruptions may have started between 8 January and 22 June 2022 – date of the first detection by *Swift*/XRT (blue points).

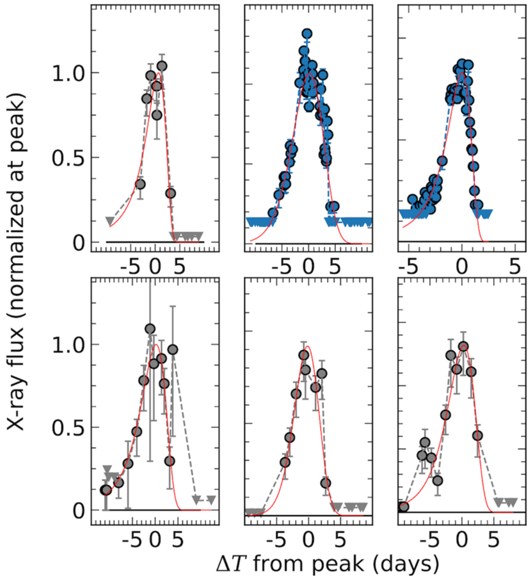

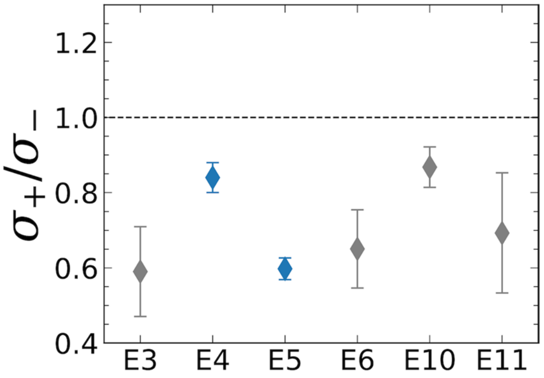

Extended Data Fig. 2 | Eruption shape fitting. Left: Fit of asymmetric Gaussian profile to the six best-sampled eruptions: around epochs *E3*, *E4*, *E5*, *E6*, *E10*, and *E11*. Right: ratio of σ_+ and σ_- showing the slight asymmetric nature of Swift J0230+28's eruption. Error-bars represent 1σ uncertainty.

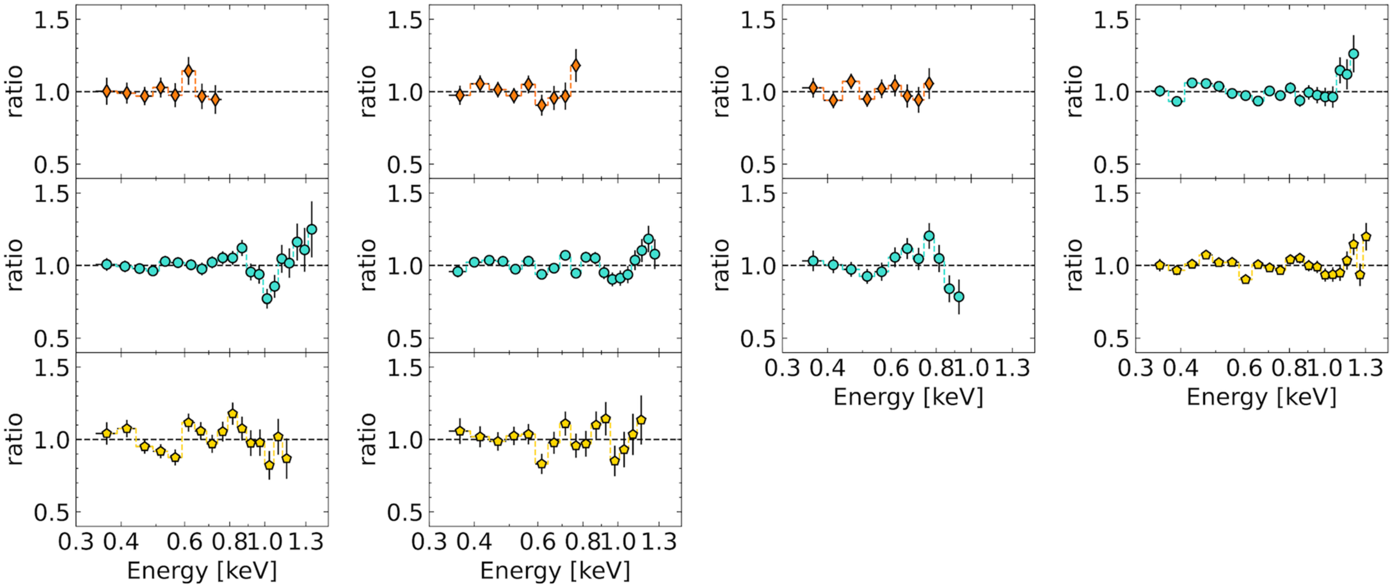

Extended Data Fig. 3 | Residuals of the stacked spectral analyses. The order (left to right panels) represent distinct eruptions while the color and vertical panels represent distinct phases of each eruption: orange (rises), cyan (peaks) and gold (decays). The order and colors are the same as in Fig. 1. Error-bars represent 1σ uncertainty.

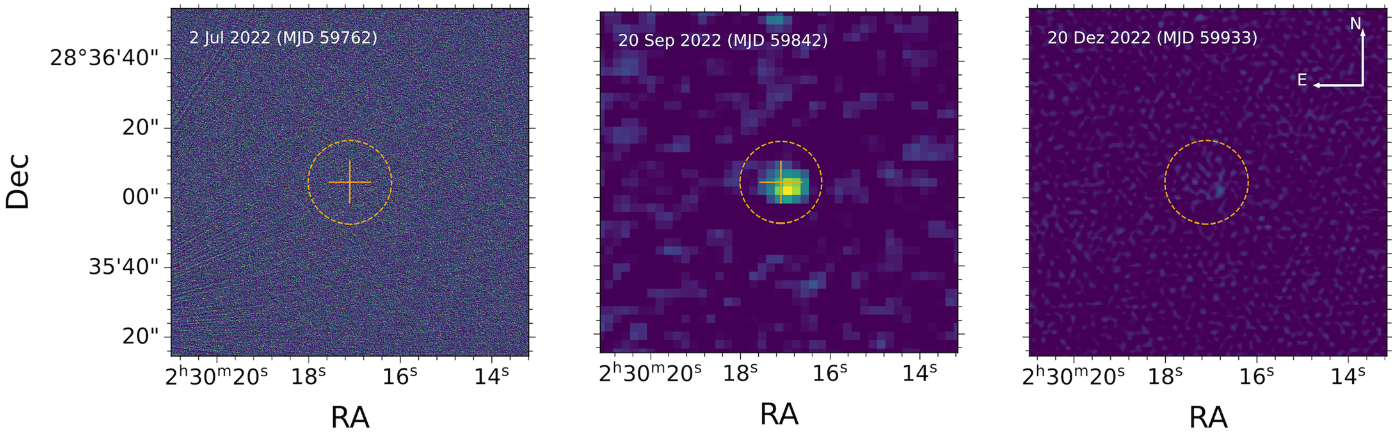

Extended Data Fig. 4 | Radio (VLA) images. A transient radio source is detected in the second radio observation (middle panel) on MJD 59842 with a flux of 93 ± 7μJy (13σ detection). No source is detected in the first and third observations (left and right panels), with upper limits of 15 μJy and 25 μJy respectively. The orange cross marks the peak of the X-ray emission, and the orange circle the Kron radius (12″) of the host galaxy.

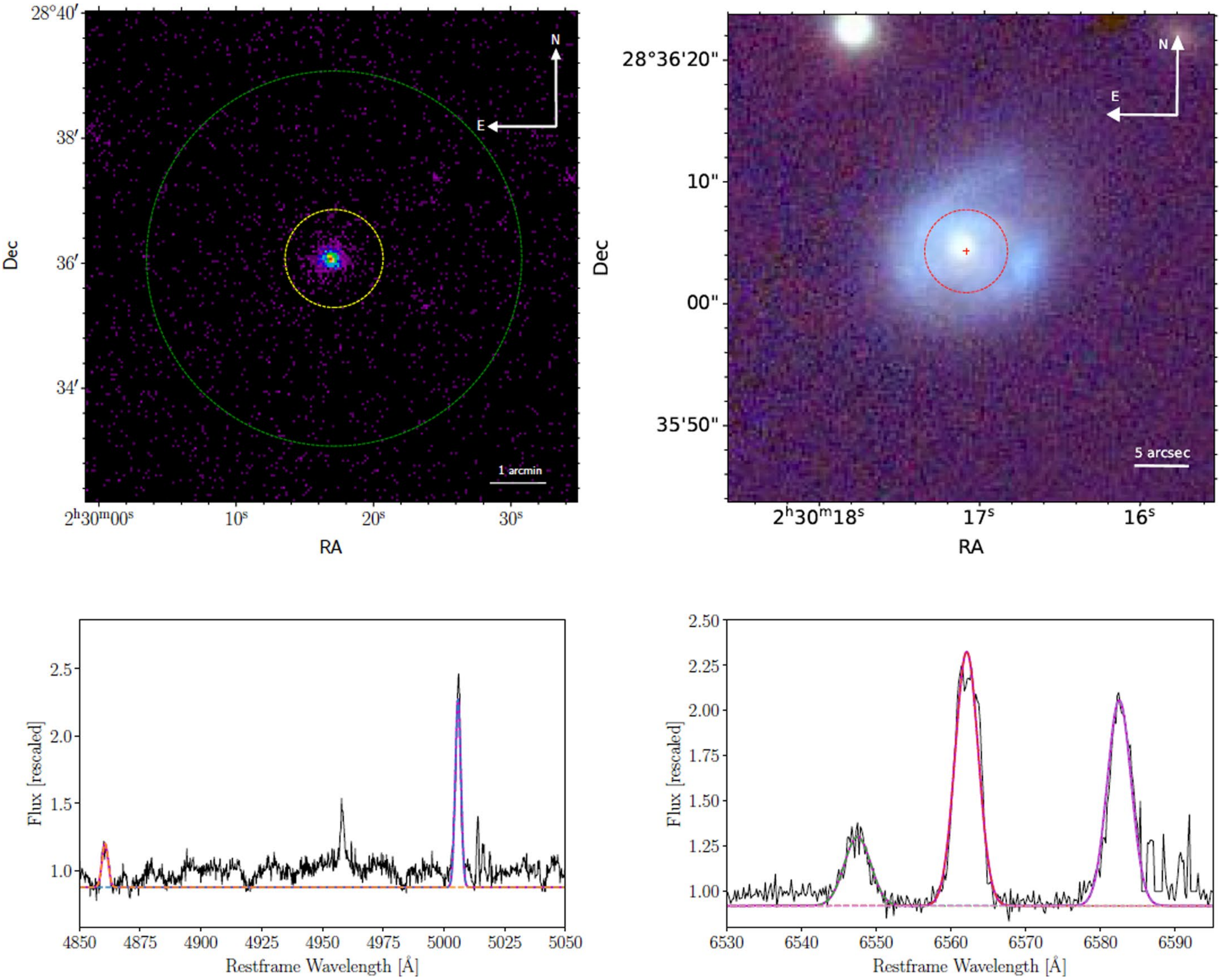

Extended Data Fig. 5 | Swift J0230+28 Position and host identification. Top left: *Swift*/XRT stacked images. Yellow 47″ circle represents the 90% region of the XRT point spread function, and was the radius used for extraction. Green circle is the *NICER* FoV, no other source is present. **Top Right**: Pan-STARRS *i*/*g*/*r* bands composed image of Swift J0230+28's host galaxy. Red cross show the location of the peak of the XRT emission and red circle (radius = 3.4″) represents the 2.7σ uncertainty on the position. The X-ray emission is consistent with the nucleus of the galaxy. **Bottom**: Continuum normalized X-shooter optical spectrum of the nuclear 1″ of the host galaxy, in the Hβ+[O III] (left) and Hα+[N II] (right) regions.

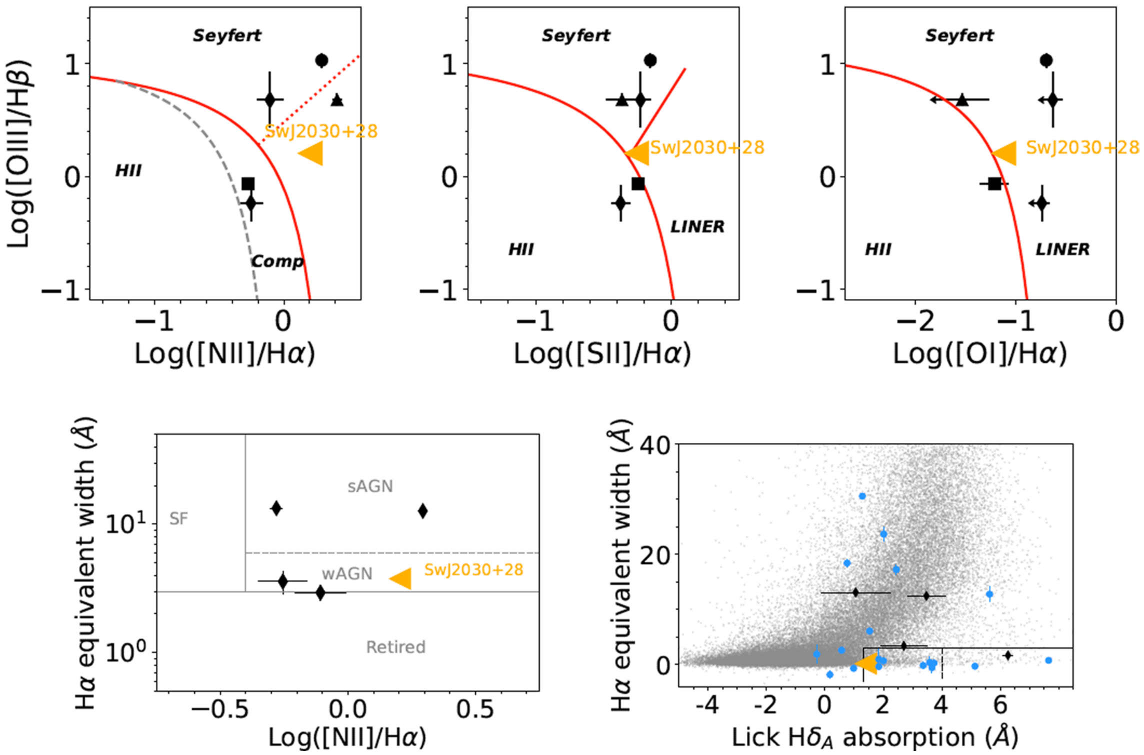

Extended Data Fig. 6 | Diagnostic diagrams of the host galaxy. Top: Swift J0230+28 in the BPT diagnostic diagram, located above the[83] theoretical upper limit for star-formation ionization (red continuous line). Black diamonds represent the 4 known QPE hosts in all panels[69]. Middle: Swift J0230+28 in the WHAN diagnostic diagram, further showing that the nucleus likely hosts a weak AGN. Bottom: the Lick Hδ absorption index as a function of Hα EW diagram. Grey points show SDSS galaxies for reference; blue circles represent TDE host galaxies. The black dash-delimited (solid) box indicates where QBS (E+A) galaxies are located. These galaxies make up 2.3% and 0.2% of the selected SDSS galaxies, respectively. Error-bars are 1σ uncertainties in all panels.

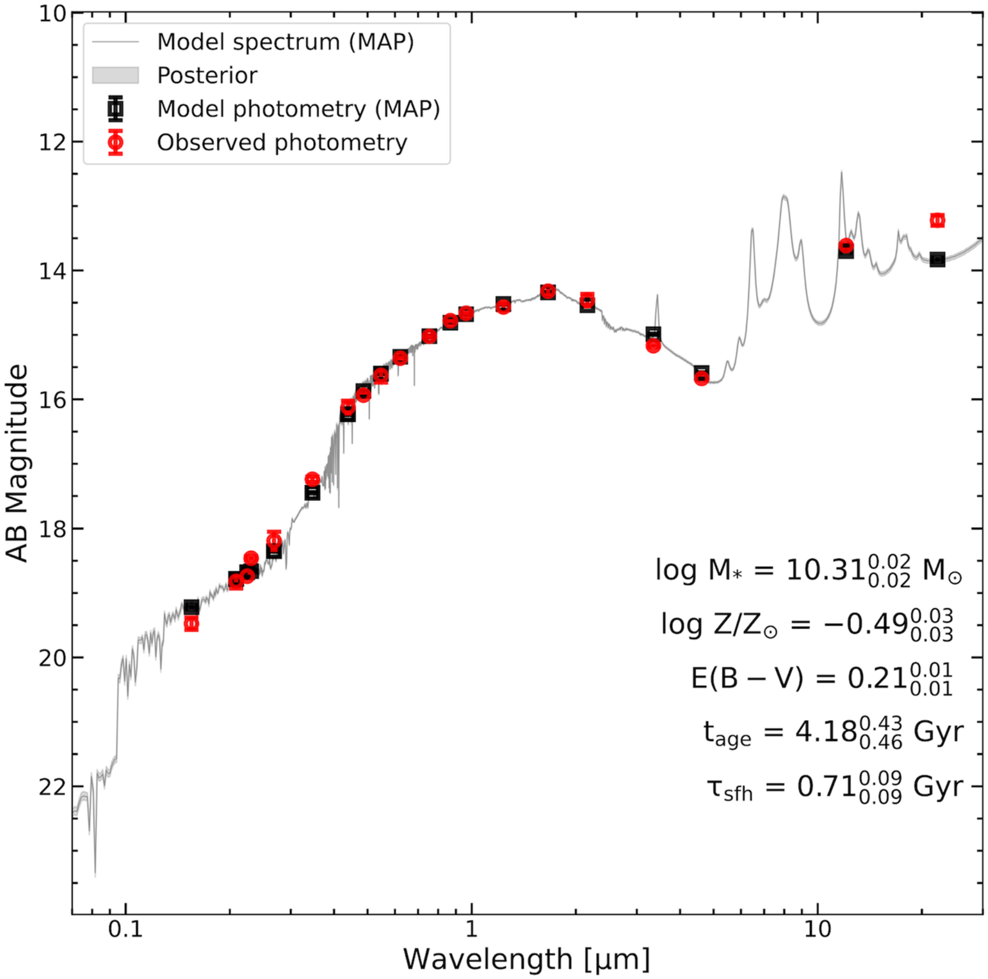

Extended Data Fig. 7 | Broad-band spectral energy distribution (SED) of host galaxy. Red points show the observed archival photometry, black point the maximum a posteriori (MAP) best-fitted mode, and grey line the MAP best-fitted spectrum. Best-fitted parameters (see text for details) for the model are shown in the lower right. Error-bars are 1σ uncertainties.

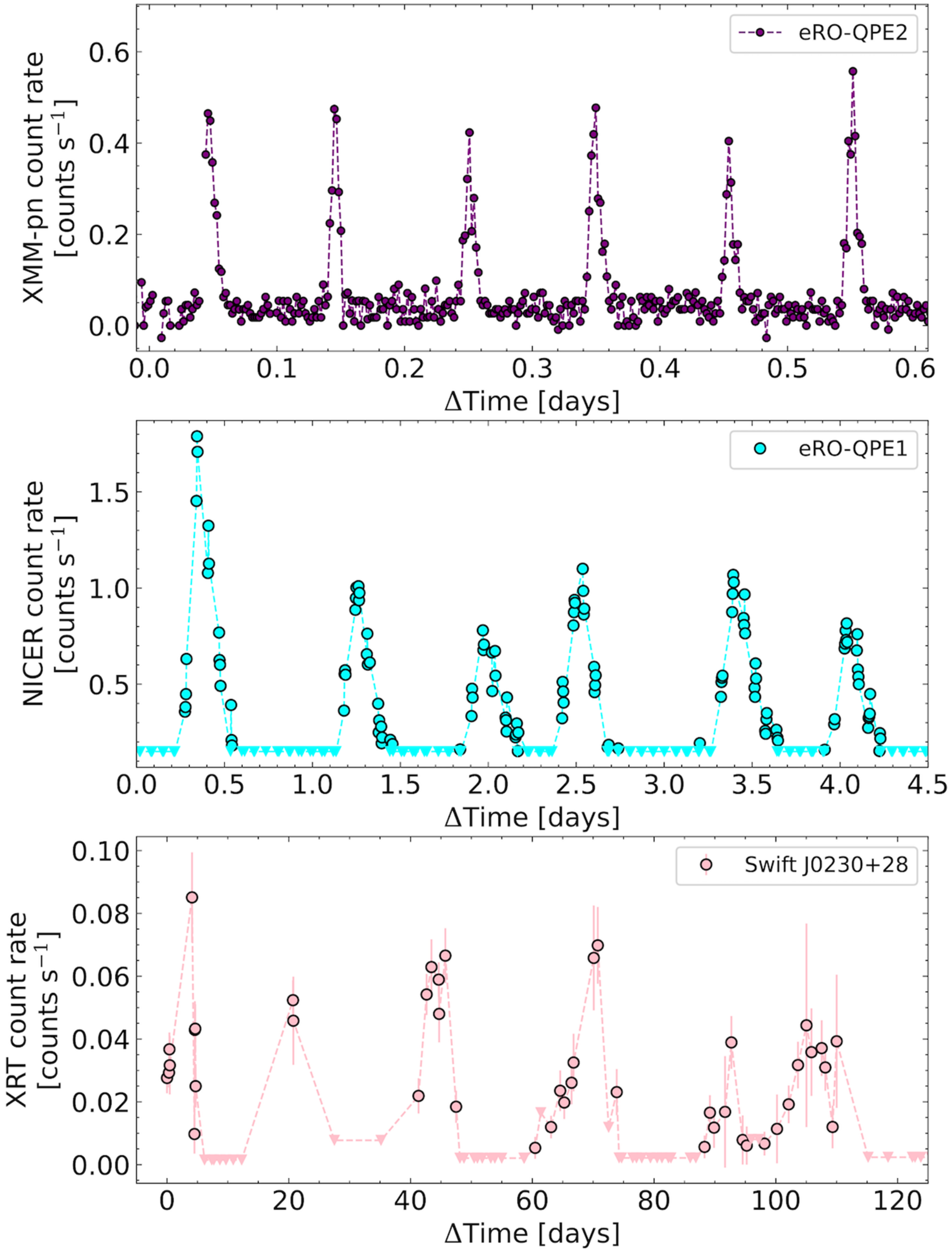

Extended Data Fig. 8 | Comparison of QPEs light curves. Top: *XMM-Newton*-pn light curve of eRO-QPE2. Center: *NICER* light curve of eRO-QPE1. Bottom: *Swift*/XRT light curves of Swift J0230+28. All three panels show six consecutive eruptions for each source, the distinct time scales are clearly given the x-axis range: 0.6 days for eRO-QPE2, 4.5 days for eRO-QPE1 and 120 days for Swift J0230+28. Error-bars are 1σ uncertainties.

Extended Data Table 1 | Summary of time-resolved X-ray spectra analyses with absorbed thermal model on stacked spectra

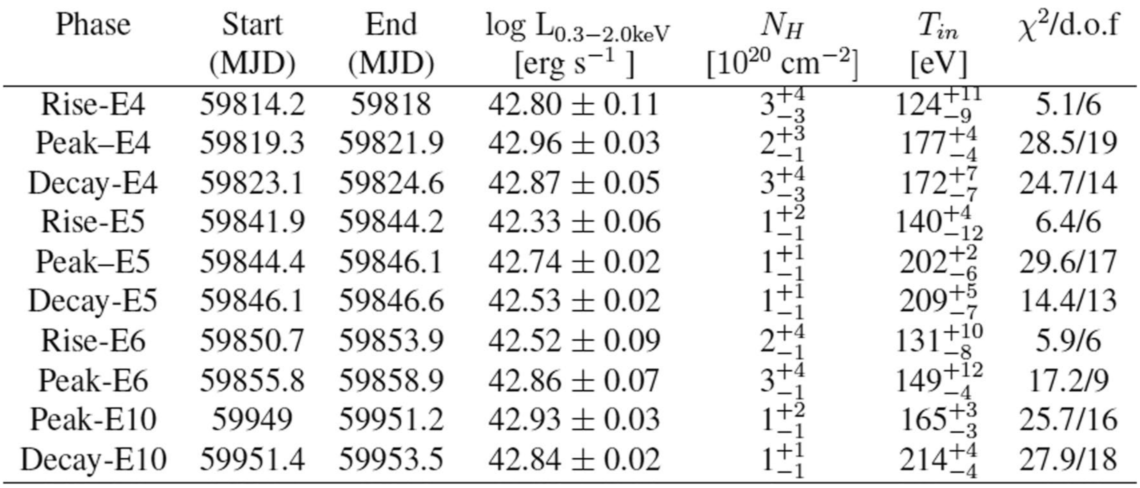

Phase	Start (MJD)	End (MJD)	log $L_{0.3-2.0\mathrm{keV}}$ [erg s^{-1}]	N_H [10^{20} cm^{-2}]	T_{in} [eV]	χ^2/d.o.f
Rise-E4	59814.2	59818	42.80 ± 0.11	3^{+4}_{-3}	124^{+11}_{-9}	5.1/6
Peak–E4	59819.3	59821.9	42.96 ± 0.03	2^{+3}_{-1}	177^{+4}_{-4}	28.5/19
Decay-E4	59823.1	59824.6	42.87 ± 0.05	3^{+4}_{-3}	172^{+7}_{-7}	24.7/14
Rise-E5	59841.9	59844.2	42.33 ± 0.06	1^{+2}_{-1}	140^{+4}_{-12}	6.4/6
Peak–E5	59844.4	59846.1	42.74 ± 0.02	1^{+1}_{-1}	202^{+2}_{-6}	29.6/17
Decay-E5	59846.1	59846.6	42.53 ± 0.02	1^{+1}_{-1}	209^{+5}_{-7}	14.4/13
Rise-E6	59850.7	59853.9	42.52 ± 0.09	2^{+4}_{-1}	131^{+10}_{-8}	5.9/6
Peak-E6	59855.8	59858.9	42.86 ± 0.07	3^{+4}_{-1}	149^{+12}_{-4}	17.2/9
Peak-E10	59949	59951.2	42.93 ± 0.03	1^{+2}_{-1}	165^{+3}_{-3}	25.7/16
Decay-E10	59951.4	59953.5	42.84 ± 0.02	1^{+1}_{-1}	214^{+4}_{-4}	27.9/18

The stacked *NICER* spectra are fit with `tbabs`*zTBabs*zashift(diskbb) model using *XSPEC*[55]. **Start** and **End** represent the start and end times (in units of MJD) of the interval used to stack the data. $\log L_{0.3-2.0\mathrm{keV}}$ is the logarithm of the integrated absorption-corrected luminosity in 0.3–2.0 keV range in units of erg s^{-1}, assuming the best-fitted model. N_H is the best-fitted intrinsic column density in units of 10^{20} cm^{-2}. T_{in} is the best-fitting inner disk temperature of `diskbb` in eV. Uncertainties represent 1σ level.

Extended Data Table 2 | Properties of Swift J0230+28 as compared to quasi-periodic eruption sources (QPEs)

Source		eRO-QPE2	GSN 069	RX J1301	eRO-QPE1	Swift J0230+28
Mean recurrence time		2.4h	9h	4.7h	18.5h	22d
Deviation from periodicity	Pattern	'long-short'		irregular		
	Absolute	2.3h-2.7h	8.5h-9.5h	3.5h-5.5h	12h-24h^a	18d-25d^b
	Fraction	$\sim\pm$ 10%		$\sim\pm$ 20%	30%-50%^{a}	$\sim\pm$ 30%^{b}
X-ray luminosity at peak^c (erg s^{-1})		$\sim 10^{42}$	$\sim 5\times10^{42}$	$\sim 2\times10^{42}$	$\sim 10^{43}$	$\sim 6\times10^{42}$
Amplitude^{c,d} (count rate)		~ 10	~ 20	~ 15	100-200	≥ 100
Temperature evolution per eruption		cool → warm → cool				cool → warm
Eruption shape		~ symmetric	~ symmetric	~ symmetric	asymmetric (longer decay than rise)	slight asymmetric (longer rise than decay)
log $M_{\rm BH}$ ($M_\odot$)		5.0 ± 0.5	6.0 ± 0.5	6.6 ± 0.4	5.8 ±0.5	6.6 ± 0.4

Notes: a) This is a conservative estimate, given that as shown by ? some of the eruptions overlap with each other, which means an even lower separation between two consecutive eruptions. b) This is a conservative estimate, based on the fitted peak (see 'X-ray light curve' in Methods) of the well-sampled eruptions, given that some eruptions were not observed around the LSP peak period (see for example, *E9* in Fig. 1), which means an even larger separation between two consecutive eruptions. c) In the 0.3-2.0 keV band. d) Defined as the ratio between count rates of the peak and quiescent states. e) Based on whether the eruptions can be well fitted by a Gaussian, or some asymmetric function, for example, asymmetric Gaussian or Gaussian-rise plus power-law decay, is necessary.